mathematics

MDPI

Article

Novel Hybrid Optimized Clustering Schemes with Genetic Algorithm and PSO for Segmentation and Classification of Articular Cartilage Loss from MR Images

Jan Kubicek *, Alice Varysova, Martin Cerny, Jiri Skandera, David Oczka, Martin Augustynek and Marek Penhaker

Department of Cybernetics and Biomedical Engineering, VŠB—Technical University of Ostrava, 17 Listopadu 2172/15, Poruba, 708 00 Ostrava, Czech Republic
* Correspondence: jan.kubicek@vsb.cz

Abstract: Medical image segmentation plays an indispensable role in the identification of articular cartilage, tibial and femoral bones from magnetic resonance imaging (MRI). There are various image segmentation strategies that can be used to identify the knee structures of interest. Among the most popular are the methods based on non-hierarchical clustering, including the algorithms K-means and fuzzy C-means (FCM). Although these algorithms have been used in many studies for regional image segmentation, they have two essential drawbacks that limit their performance and accuracy of segmentation. Firstly, they rely on a precise selection of initial centroids, which is usually conducted randomly, and secondly, these algorithms are sensitive enough to image noise and artifacts, which may deteriorate the segmentation performance. Based on such limitations, we propose, in this study, two novel alternative metaheuristic hybrid schemes: non-hierarchical clustering, driven by a genetic algorithm, and Particle Swarm Optimization (PSO) with fitness function, which utilizes Kapur's entropy and statistical variance. The goal of these optimization elements is to find the optimal distribution of centroids for the knee MR image segmentation model. As a part of this study, we provide comprehensive testing of the robustness of these novel segmentation algorithms upon the image noise generators. This includes Gaussian, Speckle, and impulsive Salt and Pepper noise with dynamic noise to objectively report the robustness of the proposed segmentation strategies in contrast with conventional K-means and FCM. This study reveals practical applications of the proposed algorithms for articular cartilage extraction and the consequent classification performance of early osteoarthritis based on segmentation models and convolutional neural networks (CNN). Here, we provide a comparative analysis of GoogLeNet and ResNet 18 with various hyperparameter settings, where we achieved 99.92% accuracy for the best classification configuration for early cartilage loss recognition.

Keywords: medical image segmentation; articular cartilage; non-hierarchical clustering; K-means; FCM; genetic algorithms; PSO

MSC: 68T20

Citation: Kubicek, J.; Varysova, A.; Cerny, M.; Skandera, J.; Oczka, D.; Augustynek, M.; Penhaker, M. Novel Hybrid Optimized Clustering Schemes with Genetic Algorithm and PSO for Segmentation and Classification of Articular Cartilage Loss from MR Images. *Mathematics* **2023**, *11*, 1027. https://doi.org/10.3390/math11041027

Academic Editor: Jakub Nalepa

Received: 22 January 2023
Revised: 10 February 2023
Accepted: 15 February 2023
Published: 17 February 2023

1. Introduction

There are various imaging systems that are used in clinical practice for articular cartilage imaging. Among the radiographic methods, the classical X-ray examination is the most important, as it provides a wide range of information about the condition of the cartilage in general and thus complements the clinical results. A significant advantage of this method is morphological imaging, which allows for the confirmation of pathological changes, the determination of their extent, and also their localization [1,2]. It is a frequently used method for imaging articular cartilage. On the other hand, this method for assessing

the state and condition of articular cartilage is highly subjective and, therefore, quite inaccurate [3,4].

Ultrasonography plays a partial role in the imaging of articular cartilage. A significant disadvantage of this imaging modality is the lack of clarity of the surrounding structures. From this perspective, it follows that this method is not clinically assessable. Ultrasonography plays an important role in the diagnosis of pre-arthritic conditions, especially in the shoulder and knee joint regions, and in the detection of effusions [5,6].

Magnetic resonance imaging (MRI) is the dominant method for joint pathology assessment. Currently, MRI is the most sensitive imaging method for joint examination. MRI sequences allow for optimized imaging of articular cartilage morphology, volumetric examinations, and biochemical analysis methods. Magnetic resonance has a high resolution, especially in terms of spatial resolution [7,8]. This capability makes it an ideal method for imaging the soft tissues of the joint and cartilage in their entirety, including any pathologies present. A significant benefit is the non-invasiveness due to the patient burden. Another advantage of modern MRI scanners is the use of sequences that allow for the optimization of cartilaginous tissue resolution. Currently, the most commonly used sequences include proton density (PD), which indicates the density of protons per unit volume, and fat-suppressed MR sequences [9,10].

Current MR imaging techniques allow for the examination of the morphological structure of cartilage. These methods are divided into conventional spin-echo (SE) sequences, gradient recall echo (GRE) sequences, fast SE sequences, and more advanced isotropic 3D SE and GRE sequences. Compositional techniques include T2 mapping, gadolinium delay-based articular cartilage imaging (dGEMRIC), T1ρ imaging, sodium imaging, and weighted diffusion imaging [11–13].

In the medical image analysis of the knee area, regional image segmentation represents an essential procedure for extracting the regions of interest, including articular cartilage, femoral, and tibial bones [13,14]. Here, the concept of regional segmentation performs a decomposition strategy, which allows for the pixel's classification into multiple segmentation classes based on the pixel's features such as intensity or geometrical characteristics. If we denote a MR knee image as $\Omega(x, y)$, where (x, y) represent the pixel's coordinates, then we can perform a decomposition of Ω into a finite number of segmentation regions: $S_k \subset \Omega,\ j, k \in \{1,\ 2,\ \ldots, n\}$, where (n) stands for the number of regions, and $(j,\ k)$ represent the region's indexes in the multiregional segmentation model. Mathematically, the regional segmentation model can be generally defined as:

$$\Omega = \coprod_{k=1}^{K} S_k,\ S_k \cap\ S_j = \varnothing \text{ for } k \neq j \tag{1}$$

Particularly, using regional segmentation methods enables a separate identification of the individual knee bones and articular cartilage [15,16]. The analysis of the cartilage is especially important due to the autonomous identification of the early pathological changes, which indicates the spots where the cartilage is missing as a result of the early osteoarthritis. Thus, a proper regional segmentation should be able to identify healthy articular cartilage from such pathological spots [17–19].

There is a wide range of regional segmentation strategies from conventional principles, including histogram partitioning, edge detection, active contours, level sets, region growing, splitting, and others, up to machine and deep learning methods. Among the principles mentioned, a very popular field of segmentation methods is based on non-hierarchical clustering with the use of K-means and its soft variant FCM, which utilize fuzzy logical rules [20–23]. Generally, these methods classify pixels based on their similarity with centroids in their respective classes and thus perform pixel assignment to regions for image segmentation. Their popularity stems from the fact that these methods can self-learn from input MR images, and not require plenty of labeled images for training as in the case of machine learning principles. On the other hand, these methods have certain

limitations, which limit their performance. Firstly, initial centroids must be selected [24]. There is no versatile approach for this task. Thus, it is standardly conducted randomly, which influences the clustering accuracy. Secondly, both concepts, K-means and FCM, are prone to noise and image inhomogeneities, which significantly influence the clustering performance for image segmentation [25,26].

Based on the aforementioned limitations of non-hierarchical clustering principles, in this study, we propose two alternative hybrid clustering principles that are based on non-hierarchical clustering with metaheuristic optimization schemes to find an optimal distribution of clusters for regional MR knee image segmentation, which should reliably identify articular cartilage and its cartilage loss. In this study, we also publish dynamical tracking of the segmentation of the robustness of knee images upon gradual image noise to objectively show the stability of the proposed hybrid segmentation methods. We put all the results in contrast with K-means and FCM-based clustering to report differences with classical methods of non-hierarchical clustering. Based on the segmentation models of articular cartilage, we provide a comparative analysis of two convolutional neural networks (CNN), including GoogLeNet and ResNet 18, for distinguishing healthy cartilage and early signs of osteoarthritis (cartilage loss). The classification procedure objectively shows the potential for successful recognition of early osteoarthritis based on the proposed segmentation procedures. This study brings the following novel facts:

- Two hybrid segmentation schemes of non-hierarchical clustering driven by genetic algorithms and PSO;
- Extraction and modeling articular cartilage using the proposed schemes;
- Analysis of the robustness of the proposed schemes based on noise generators with dynamic intensity;
- Classification analysis performance to recognize early osteoarthritis based on segmentation models with CNN architectures.

The rest of the paper is organized as follows: in the second section, we publish the recent state-of-the-art notes on articular cartilage segmentation and modeling; the third section is focused on the design and implementation of novel clustering-based segmentation methods for multiregional segmentation; the fourth section deals with the analysis of the segmentation performance and classification of early cartilage loss; and the last section deals with the discussion and future perspectives of this study.

2. Recent Work

In this section, we present the essential facts about articular cartilage segmentation with the goal of recognizing it and cartilage loss from MR images. In principle, the segmentation methods may be categorized based on the level of the user's intervention during the segmentation process. Here, we can recognize the principles of manual, semiautomatic, and fully automatic segmentation methods.

Previous studies have shown that the development of fully automatic algorithms for articular cartilage segmentation is not a trivial task, especially due to the variability of MR sequences and different manifestations of cartilage features. Therefore, in some studies, the manual contouring of articular cartilage boundaries by an expert takes the most used techniques to extract cartilage features [27,28]. Additionally, such manual contouring plays an important role in the evaluation of segmentation performance using ground truth data. It is a highly laborious and time-consuming procedure that can represent a time burden of several hours for the analysis of a single knee recording, depending on the image size, quality, and disease state of the individual patient. Moreover, this method lacks relevant reproducibility due to human subjective error and requires special training and experience [28–30]. However, none of the existing (semi)automatic algorithms have been able to provide visually pleasing results, and thus manual segmentation persists as the gold standard for validating segmentation algorithms [31,32].

The major current trends in the segmentation of articular cartilage are focused on the development of automatic algorithms that are capable of autonomously identifying

cartilage morphologic features from MR images. An ideal segmentation algorithm should maximize precision and accuracy for large-scale variant image outputs while keeping user interaction to a minimum [33]. The main goal is to develop fully automatic segmentation algorithms possessing high cartilage localization accuracy, specificity, reproducibility, robustness, and a reasonable computational time. This task is complicated by many subfactors [33,34].

The articular cartilage layer is very thin, in some areas reaching sub-millimeter levels. It is therefore required to achieve the most relevant segmentation possible, where only high-resolution MR images can be used as a source, although this requirement is associated with relatively high acquisition times [35]. As the amount of time a patient spends in the gantry increases, the risk of inadvertent patient movements causing image artifacts increases, posing a significant problem in terms of classifying areas of articular cartilage and differentiating surrounding tissues [35,36].

Achieving a sufficient contrast between the articular cartilage and the surrounding tissues, especially the bone, is also a significant issue. Even after fat suppression, the boundary between cartilage and ligaments or fatty tissues is very vague. An important fact that should be mentioned is that the cartilage tissue is not homogeneous throughout. Therefore, the algorithm should be trained to recognize these patterns in order to achieve maximum robustness [37,38]. Image noise is another factor that has a direct effect on the segmentation output. A simple principle applies, which points out that the relevance of segmentation quality depends on the quality of the input image data [39,40].

The recent trends for automatic cartilage modeling and extraction mainly follow methods using artificial intelligence. Here, neural network architectures are frequently used [41–45]. Recent studies mostly suggest using the principles of convolutional neural networks and deep learning principles such as U-net for articular cartilage segmentation and classification [46–49].

In contrast with such intelligent principles, there are also self-learning strategies such as non-hierarchical clustering (K-means, FCM, and their variants), which do not require plenty of labeled image data for training such supervised methods. Since these methods have limitations in the definition of cluster centroids and they are prone to image noise, as we stated earlier, there is a strong potential for developing hybrid methods of clustering driven by optimization schemes to increase the accuracy and robustness of the image segmentation in various image conditions. This study is focused on revealing hybrid clustering schemes with metaheuristic optimization algorithms to prevent the standard drawbacks of clustering methods and provide robust and efficient segmentation of the knee area from MR images.

3. Materials and Methods

In this section, we present proposed hybrid systems for MR knee image segmentation and extraction of articular cartilage, which are consequently used for the classification of the early signs of osteoarthritis with cartilage loss from the healthy cartilage.

The core of segmentation methods is non-hierarchical clustering based on the K-means clustering principle. This method has been frequently used in various studies for the purpose of regional segmentation. The limitation of this method is the selection of initial centroids, representing etalons for each cluster (segmentation class). The task of this selection is standardly conducted by the randomized distribution of clusters in the feature's space. This is an inappropriate method because the initial clusters may be badly selected and far from the real centroids of segmented regions. Thus, K-means is not able to correctly find the convergent solution for the segmentation model. In such cases, more tissues, such as parts of bones and cartilage, may be joined together, which limits proper segmentation. Additionally, the final segmentation via clustering is also prone to image noise, artifacts, and other spatial image parameters that may affect the image intensity distribution. Based on these facts, we present novel optimization schemes, which are supposed to find the

optimal configuration of the centroid's distribution for non-hierarchical clustering based on metaheuristic genetic algorithms and PSO.

In this study, we provide testing of various settings of these optimization schemes in contrast with standard K-means and FCM for regional segmentation of knee MR images to demonstrate that metaheuristic optimization has the potential to outperform conventional non-hierarchical clustering-based segmentation. We provide the mentioned testing procedures by applying the noise generators (Gaussian, Speckle, and Salt and Pepper noise) with dynamic noise intensity to track the robustness of individual segmentation methods for MR knee image decomposition. The segmentation accuracy for each noise level is objectively evaluated based on the following parameters: mean squared error (MSE), index of correlation (Corr), structural similarity (SSIM), and Jaccard coefficient (JC).

Consequently, we use the proposed hybrid segmentation schemes for the extraction of articular cartilage. Here, the proposed segmentations should reflect the healthy structure of cartilage and pathological cartilage loss from osteoarthritis. To objectively evaluate the recognition of cartilage structure from the proposed models, we incorporate the classification procedures based on convolutional neural networks (GoogLeNet and ResNet 18) with various hyperparameter settings to find optimal settings of CNN, which best classifies healthy segmented cartilage from cartilage loss.

3.1. Initialization and Definition of Clustering Strategies

In this section, we introduce individual clustering strategies, which are used for MR image segmentation with the goal of identifying morphological features of articular cartilage. As we stated earlier, in this study, we propose novel hybrid schemes for the optimization of a conventional K-means-based strategy with two strategies based on the genetic algorithm and evolutionary strategy PSO.

Both optimization strategies are aimed at finding the best configuration of clusters, which will reliably reflect the multiregional segmentation model of knee MR images. Generally, the image is supposed to be decomposed into a predefined number (n) of segmentation classes to identify individual tissues such as bones, cartilage, ligaments, and others. The proposed strategies generate a set of initial combinations of centroids, which are generated randomly. This operation can be represented by a random matrix (C_R) of initial centroids, where each row represents one possible configuration of centroids:

$$C_R = \begin{bmatrix} C^1_{R,1}, & C^1_{R,2}, \ldots, & C^1_{R,n} \\ C^2_{R,1}, & C^2_{R,2}, \ldots, & C^2_{R,n} \\ & \cdot & \\ & \cdot & \\ & \cdot & \\ C^p_{R,1}, & C^p_{R,2}, \ldots, & C^p_{R,n} \end{bmatrix} \tag{2}$$

which generates (p) random configurations of centroids (C) for a multiregional segmentation model with (n) clusters. Here, $n \in \mathbb{Z}$, in the range: $[2; I_{max}]$ where I_{max} stands for the maximum intensity of the MR image. Note that we use 8-bit images ($I_{max} = 256$) in this study. The configuration (n = 1) would not make sense because all the pixels would be classified into a single cluster.

After this initial phase, where a set of possible solutions (C_R) of centroids is generated, the initial classification of pixels to individual centroids for each centroid's configuration

is conducted based on the minimal Euclidean distance (Ed) between cluster and pixel (r), which may be represented by the equation:

$$r_* = \begin{bmatrix} min\left(Ed_1^1\left(r, C_{R,1}^1\right),\ Ed_2^1\left(r, C_{R,2}^1\right), \ldots, Ed_n^1\left(r, C_{R,n}^1\right)\right) \\ min\left(Ed_1^2\left(r, C_{R,1}^2\right),\ Ed_2^2\left(r, C_{R,2}^2\right), \ldots, Ed_n^2\left(r, C_{R,n}^2\right)\right) \\ \vdots \\ min\left(Ed_1^p\left(r, C_{R,1}^p\right),\ Ed_2^p\left(r, C_{R,2}^p\right), \ldots, Ed_n^p\left(r, C_{R,n}^p\right)\right) \end{bmatrix} \quad (3)$$

By this principle, each pixel is classified as the cluster in each set of centroids (p) based on its minimal Euclidean distance, where the symbol (*) stands for the index of the cluster with the minimal distance to the pixel (r). This approach forms the initial assignment of pixels into randomly selected clusters. This initial set of cluster formations is the input for the optimization strategies based on the genetic algorithm and PSO to find the best clustering model for MR image segmentation. The whole segmentation strategy based on the optimized clustering schemes with the genetic algorithm and PSO is illustrated in Figure 1.

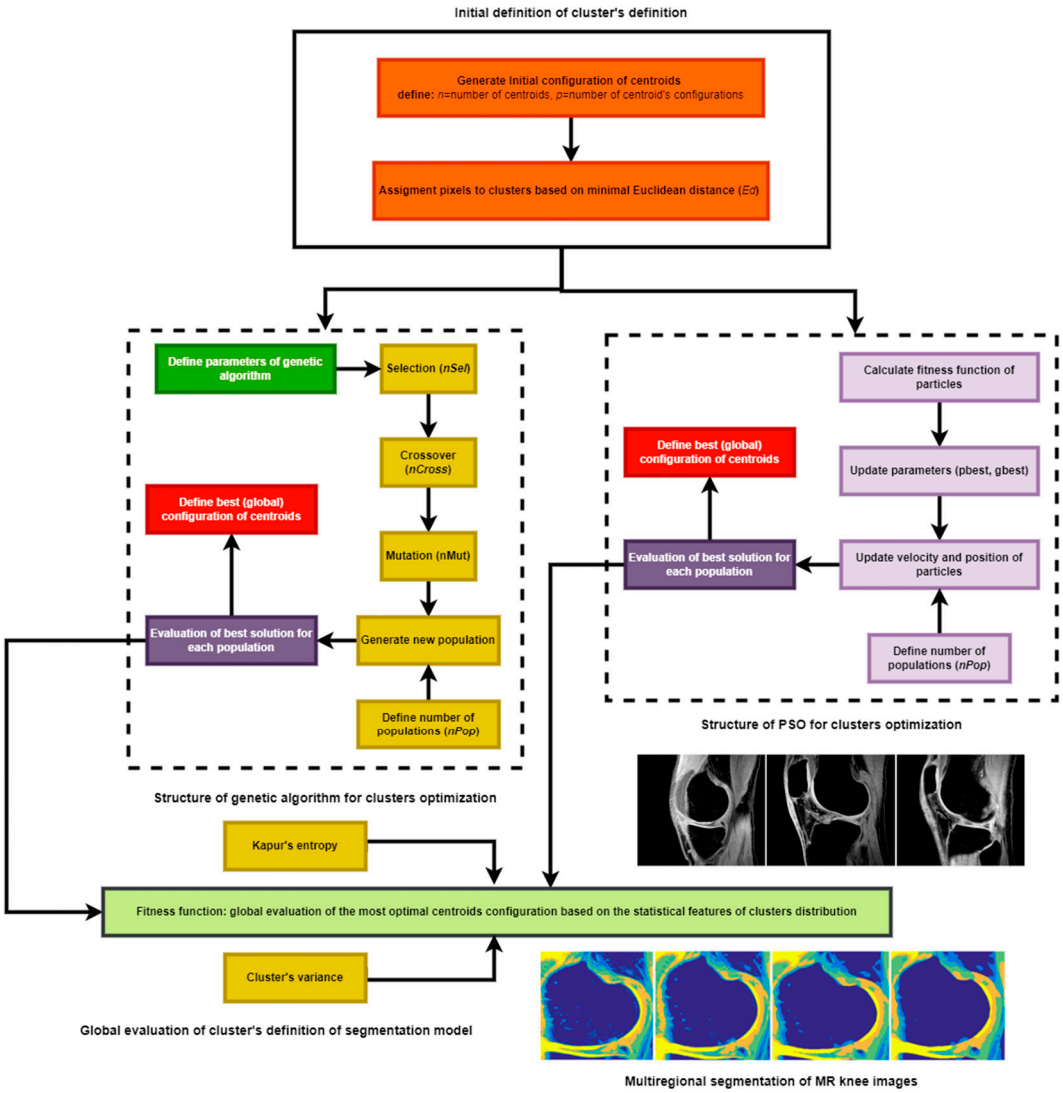

Figure 1. Complex general flowchart of an optimized clustering strategy with genetic algorithm and PSO for multiregional segmentation of MR knee images.

The optimization schemes (Figure 1) have the task of selecting the most optimal solution for the distribution of centroids with classified pixels from individual tested variants within a predefined number of populations (*nPop*).

The most important procedure in the optimization process is the evaluation of the quality of each solution for centroids distribution. There should be a distribution of centroids for each single tested solution in the optimization, which is called a chromosome. Pixels are classified to each centroid based on the minimal Euclidean distance (Equation (3)). Thus, each chromosome is formed by (n) clusters of pixels. In each population, we define (p) such configurations (chromosomes). In order to evaluate the quality of each possible centroid solution, we define a fitness function that evaluates the homogeneity and compactness of the cluster's configuration based on Kapur's entropy and variance for each cluster. We describe this in further detail.

The result of these optimization procedures and further application of non-hierarchical clustering based on the principle of K-means can be understood as the form $\{Cl_1(C_1, r_1),\ Cl_2(C_2, r_2), \ldots, Cl_n(C_n, r_n)\}$. This form generates the (n) regional segmentation model, where each region (cluster—Cl) is specified by its centroid (C) and a finite set of pixels ($r \in Cl$).

After the optimization procedure is concluded with the definition of centroids ($\{C_1,\ C_2, \ldots, C_n\}$), non-hierarchical clustering is applied. Here, these centroids are utilized as the initial etalons of the clusters, which will represent individual segmentation regions. Consequently, each pixel is classified as the centroid with minimal Euclidean distance. Therefore, new centroids are calculated from the pixels for each cluster, and the pixel's assignment is computed for the new centroids. The algorithm falls into convergence when, in two consecutive iterations, there is not any pixel reclassification between clusters as there is in conventional K-means.

3.2. Genetic Algorithm for Non-Hierarchical Clustering

Genetic algorithms are based on Charles Darwin's model of the theory of natural evolution. The algorithms reflect the overall process of natural selection and simulate the struggle for the survival of individuals. Individuals with the most suitable traits are selected for subsequent reproduction to produce better offspring in the next generation. They belong to the group of evolutionary algorithms, which, unlike traditional algorithms, are dynamic and can therefore evolve over time.

The genetic algorithm process consists of the following steps: initialization, evaluation, crossover, mutation, and selection. The process is initially given by a random group of individuals, which we call a population. Each individual is the result of the problem we want to solve. Individuals are characterized by a set of parameters called genes. The joining of individual genes into a chain forms the basic element of a biological population called a chromosome.

In our implementation, we use three biologically based operators (selection, crossover, and mutation) to select the based chromosomes for optimal cluster configuration. For the selection operator, we implemented a roulette selection, which represents a stochastic process where the selection probability of a chromosome is proportional to its fitness function. Here, we implemented a weighted version of roulette selection, where the chromosomes with a higher fitness function value will likely be selected for the selection. In the population with (p) chromosomes, for each such chromosome (x) with corresponding fitness function fit_x we compute the probability p_x, indicating that the chromosome will be considered:

$$p_x = \frac{fit_x}{\sum_{i=1}^{p} fit_i} \tag{4}$$

This way, we obtain the probability distribution: $P = \{p_1,\ p_2, \ldots, p_p\}$. From this distribution, we select (*nSel*) chromosomes with the highest probability.

The second genetic operator we use in the proposed optimization scheme is crossover with the steering parameter (*nCross*), which determines a percentual ratio of the chromo-

somes that will be crossed to produce new offspring. To ensure a better quality of the candidates, we select (*nCross*) candidates based on their probability (*P*), which reflects their quality. These candidates are grouped into couples, where each couple generates a new candidate containing a random 50% of centroids from each crossed candidate.

The last genetic operator in this optimization scheme is the mutation with steering parameter (*nMut*). This parameter determines the percentual ratio of the candidates to which the mutation is applied. As well as in the previous case, we select (*nMut*) candidates based on their probability (*P*) to ensure a better quality of candidates. The operator mutation is tasked with randomly modifying 30% of the centroids from the selected chromosomes, thus generating new candidates. After this concluding step in the genetic algorithm, the optimization procedure generates the best solution (the centroid's configuration) for a population based on the fitness function, which is stored in the memory. This procedure is repeated for the entire population so that the best centroid configurations, which the optimization procedure was able to find, can be stored.

These described procedures are applied to the chromosomes of each population. Finally, from each population, the chromosome with the highest fitness function value is selected. This procedure is repeated for all the populations (*nPop*). Thus, we completely have *nPop* candidates, where the final selection is based on the maximal value of the fitness function.

3.3. Particle Swarm Optimization (PSO) for Non-Hierarchical Clustering

Particle Swarm Optimization (PSO) is an evolutionary algorithm created by Eberhart and Kennedy in 1995. It finds inspiration in biological processes such as the behavior of schools of fish and birds. The principle is to send a population of particles into space, where each particle flies through at a certain speed. In each step, an individual velocity is determined for each particle based on the position of the best particle as well as the particles in its vicinity. In addition, the particle velocity is dynamically adjusted from time to time according to its own experience and information shared among the other particles in its neighborhood. A problem-specific criterion called the fitness function is used to evaluate the current position of all particles and guides the swarm to fly to the best location. If the position and velocity of the *i*-th particle in the *i*-th iteration are represented by $x_i(t)$ and $v_i(t)$, they are updated as follows:

$$x_i(t+1) = x_i(t) + v_i(t+1) \tag{5}$$

$$v_i(t+1) = \omega \cdot v_i(t) + c_1 \cdot r_1 \cdot (pbest_i(t) - x_i(t)) + c_2 \cdot r_2 \cdot (gbest(t) - x_i(t)) \tag{6}$$

where $(pbest_i(t))$ is the best previous position (*i*) of the particle or the value of the fitness function, ($gbest(t)$) is the global best position among all particles. (c_1) and (c_2) are the two positive learning factors, (r_1) and (r_2) are uniformly distributed random numbers taking the interval <0,1> and (ω) is the inertial mass coefficient used to control the impact of the particle's previous velocity between 0 and 1. The part of the equation $v_i(t+1)$ is called the inertia since it represents the particle's motion in the original direction; this parameter can be multiplied by a certain weight.

3.4. Fitness Function

As we already stated earlier, each candidate solution (chromosome) is evaluated with the optimization process based on the fitness function, which determines the homogeneity and compactness of individual clusters and the whole clustering model. The proposed form of the fitness function is designed based on computing Kapur's entropy and variance for each cluster as the contribution for the entire clustering scheme.

Here, Kapur's entropy [50] is aimed at measuring the compactness of each defined cluster. Therefore, the fitness function is aimed at maximizing Kapur's entropy to obtain the clusters containing concentrating pixel values around the cluster's centroid without

outliers; the intensity features would badly correspond with the cluster's distribution. Thus, we can define Kapur's entropy for the entire clustering model in the form:

$$\mathrm{H}(Cl_1,\ Cl_2,\ldots,Cl_n) = \sum_{\mathrm{i}=0}^{n} \mathrm{H}_i \tag{7}$$

where $\left(\mathrm{H}_{(*)}\right)$ stands for Kapur's entropy for the respective region. Based on this definition, Kapur's entropy can be defined for the segmentation region as:

$$\mathrm{H}_n = -\sum_{i=1}^{N_n} \frac{p_i}{\omega_0} ln\left(\frac{p_i}{\omega_0}\right),\ \omega_0 = \sum_{i=1}^{N_n} p_i \tag{8}$$

Through this method, Kapur's entropy is computed for each cluster with $(N_{(*)})$ pixels with the assumption: $N = \sum_{i=1}^{N_n} N_i$, where (N) stands for total number of pixels in the MR image.

The second feature that has the potential to evaluate the properties of clusters and is used in the proposed form of the fitness function is a cluster's variance. In addition to the compactness computed by Kapur's entropy, variance is here perceived as a statistical operator that can evaluate a concentration of pixels that belong to a respective region. Such variance contributions from all the regions are further summed up for the final variance for the entire clustering model. Since variance evaluates the level of intensity distraction inside the cluster and then quantifies homogeneity, the use of the fitness function is attempted to minimize variance for the clustering model. Variance is computed as a sum of quadratic differences for each pixel and centroid, where variance contributions are summed up to determine the final variance for the entire (n) clustering model.

$$\sigma^2(Cl_1,\ Cl_2,\ldots,Cl_n) = \sum_{\mathrm{i}=0}^{n} \sigma_i^2 \tag{9}$$

$$\sigma_i^2 = \frac{1}{n_i} \sum_{k=1}^{n_i} (r_k - C_k)^2 \tag{10}$$

Here, (σ_i^2) stands for the variance of the i-th region, containing (n) pixels (r) and the centroid (C). Based on Kapur's entropy and variance, we propose the fitness function $(fit_{(*)})$, which is applied to each considered chromosome to recognize its local quality within the global optimization task. The higher the fitness function chromosome's value, the better quality is achieved. The fitness function of the chromosome (x) with (n) clusters is defined as follows:

$$fit_x = \frac{\sum_{\mathrm{i}=0}^{n} \mathrm{H}_\mathrm{i}}{\sum_{\mathrm{i}=0}^{n} \sigma_i^2} \tag{11}$$

3.5. Interpretation of Segmentation Model

The previous subsections describe the composition of two optimized clustering schemes, which are interpreted by a set of centroids and the pixels, which are classified into individual centroids. Such a model is further used for making a segmentation model that is supposed to reflect and differentiate individual tissues in MR knee images to recognize articular cartilage from the rest of the knee area. To make such a multiregional segmentation model, we performed so-called labeling of the pixels belonging to the same cluster to make them recognizable from other regions. This labeling assigns the pixels from the same cluster a unique number (label). Furthermore, each such single label is given a single color to be visually recognized as individual tissues, which are separated into individual clusters. Note that this operation represents the transformation of individual intensity levels into unique cluster labels. Mathematically, it has the form of an indexed matrix, where the index is perceived as the mentioned label.

3.6. Dynamical Features of Segmentation Model

In this subsection, we focus on the methodology that evaluates the quality of segmentation, which is a crucial task for reporting on the segmentation performance. The segmentation performance is conducted based on the gradual degradation of native MR images with various image noise generators with gradually increasing intensities. For all the noise intensities, we computed segmentation models, which are objectively compared against the same segmentation from native images without noise. This analysis enables an objective view of the dynamic trend of performance characteristics for individual clustering methods from the perspective of their performance's stability over image gradual deterioration. This enables a comparison of the proposed optimized schemes based on the genetic algorithm and PSO with conventional K-means and FCM. Practically, we provide the analysis of robustness for the noise generators, including Gaussian noise, Speckle noise, and Salt and Pepper (impulsive) noise.

Gaussian noise represents a noise type in the image that appears as statistical white noise. This noise arises naturally in the environment where the radio diagnostic instrument is scanning and is caused, for example, by the ambient temperature. The name "Gaussian noise" comes from its distribution, which corresponds to a Gaussian normal distribution, or the noise in the image is uniformly distributed, and the pixels have the same noise intensity. Gaussian noise is expressed as follows:

$$G(x) = \frac{1}{\sigma\sqrt{2\pi}} e^{\frac{(x-\mu)^2}{2\sigma^2}} \tag{12}$$

where (x) is the brightness of the noise, (σ^2) represents the variance, and (μ) is the mean. The variance and mean are the input parameters for the noise implementation.

Speckle noise commonly arises when images are taken using so-called coherent imaging systems. This group of imaging methods includes, for example, lasers, acoustic systems, and ultrasounds. Speckle noise is caused by the interference of a signal returning from a target with a different phase. The noise is observable in the image as dark pixels possessing a higher brightness value. The parameter for adjusting the magnitude of the noise is the noise variance. This noise can be expressed as:

$$J = I + n * I \tag{13}$$

where (I) is the original input image, (J) represents the noise distribution in the input image, and (n) represents the unified zero mean value of the noise in the input image.

Salt and Pepper noise is characterized by its occurrence during data transmission. This noise is manifested by pixel degradation at several points in the image, where the new pixel contains no information about the original brightness value. This is called impulse noise. As the name implies, this noise manifests itself as black and white pixels in the image represented by the values 0 and 255. These new pixels resemble salt and pepper. In this noise, we set the parameter density (d), which represents a ratio of pixels that are affected by the noise.

3.7. Objective Evaluation of Segmentation Performance

In this subsection, we introduce the evaluation parameters considered for the quality of segmentation evaluation. We use reference-based parameters, which utilize the segmentation of native MR images as a reference against individual segmentation from the same MR images but are affected by the noise of a specific intensity. Through this method, we objectively evaluate the dynamical features of proposed optimized segmentation methods against the conventional K-means and FCM. In the section results, we introduce evaluation characteristics for evaluation parameters, which objectively show and compare the segmentation performance under gradual image degradation. The following parameters are considered for objective evaluation.

The Structural Similarity Index (*SSIM*) [51] is based on the calculation of three image components: brightness, contrast, and texture. The total index is a multiplicative combination of these three components. This provides information about the scene structure in the image. The result takes an interval from -1 to 1, where a value of 1 represents duplicate images. The calculation of the metric is shown by the formula:

$$SSIM\,(x,y) = \frac{\left(2\mu_x\mu_y + C_1\right)\left(2\sigma_{xy} + C_2\right)}{\left(\mu_x^2 + \mu_y^2 + C_1\right)\left(\sigma_x^2\sigma_y^2 C_2\right)} \tag{14}$$

where $C_{1,2} = (k_{1,2},\ L)^2$, (L) represents the dynamic range of pixel values, $k << 1$ are small constants usually with values of 0.02, (μ) represents the weighted average of (x) and (y) images, and (σ) represents the covariance of (x) and (y).

The correlation coefficient (*Corr*) describes the degree of linear correlation between two images. The coefficient can take values from -1 to 1, with 1 indicating the highest possible match between the two images. The principle is to calculate the difference in intensity values of each pixel in the two images relative to the overall average intensity of the whole image. The variables (m) and (n) represent the position of the pixel in the image. The calculation of the metric is represented by the formula:

$$Corr = \frac{\sum_m^n \sum_n \left(A_{mn} - \overline{A}\right)\left(B_{mn} - \overline{B}\right)}{\sqrt{\left(\sum_m \sum_n \left(A_{mn} - \overline{A}\right)^2\right)\left(\sum_m \sum_n \left(B_{mn} - \overline{B}\right)^2\right)}} \tag{15}$$

where $(\overline{A})$ and $(\overline{B})$ represent the arithmetic mean for each of the images (A) and (B).

The Mean Squared Error (*MSE*) is one of the conventional and simple ways to determine the degree of difference between two images. It involves calculating the average sum of the squares of two different image pixels. The *MSE* value indicates the average difference of pixels in the whole image. A higher *MSE* value indicates a greater difference between the original and processed images.

The drawback of the method is the difference in grayscale, where the value always has the same weight. In cases where the background of the image is noisy, the mean square error evaluates a higher *MSE* even if the object in the image is well recognizable. The calculation of the metric is represented by the formula:

$$MSE = \frac{1}{MN}\sum_{i=1}^{M}\sum_{j=1}^{N}\left(x_{i,j} - y_{i,j}\right)^2 \tag{16}$$

where (M) is the image size in the horizontal direction, (N) is the image size in the vertical direction, $\left(x_{i,j}\right)$ corresponds to a pixel in the segmented image with additive noise at coordinates (i) and (j), and $\left(y_{i,j}\right)$ corresponds to a pixel in the gold standard at coordinates (i) and (j).

Jaccard's coefficient (*Jaccard*), also known as IoU (Intersection-Over-Union), is one of the most commonly used metrics in determining the output quality of segmentation. The Jaccard coefficient emphasizes the similarity between finite sets of pixels and is formally defined as the size of the intersection divided by the union size of each set of pixels. This metric ranges from 0 to 1, with 0 indicating an absolute mismatch in overlap and 1 indicating perfectly overlapping segmentation. The computation of the metric is shown by the following formula, where (A) represents the image after segmentation with additive noise and (B) represents the gold standard. The numerator represents the overlap region, and the denominator represents the fusion region of the images.

$$Jaccard = \frac{|A \cap B|}{|A \cup B|} = \frac{|A \cap B|}{|A| + |B| - |A \cap B|} \tag{17}$$

The full name of the Sørensen Dice coefficient (*Dice*) is the double overlap area divided by the total number of pixels in both images. The Dice coefficient is very similar to Jaccard's. They are both positively correlated, meaning that if one says that model (A) is better than model (B) in the segmentation evaluation, then the other will say the same. As with the Jaccard coefficient, both range from 0 to 1, with 1 indicating the greatest similarity between the predicted and true predictions. A value of 1 represents a complete overlap of images. A value of 0 represents that there is no spatial overlap between two images after binary segmentation. The calculation of the metric is shown by the formula:

$$Dice = \frac{2 \cdot |A \cap B|}{|A| + |B|} \tag{18}$$

4. Results

In this section, we introduce and analyze the results of our study. Here, we provide a description of the MR datasets of the knee area that were used for this study. The optimized methods introduced in the previous section are here used for the segmentation of the knee area to extract articular cartilage and other tissues. We analyze the dynamical effect of various noise generators on the quality of segmentation to objectively report segmentation performance under gradually worse image conditions. These characteristics are supposed to indicate the performance of the proposed optimized clustering methods in comparison with conventional clustering strategies. Lastly, we show the utilization of segmentation of articular cartilage to recognize the early stage of osteoarthritis via convolutional neural networks.

4.1. MR Knee Images

In this subsection, we introduce the MR image dataset, which we used for the analysis of segmentation performance and consequently for the classification of early cartilage loss. There are various imaging systems that are clinically used for knee area and articular cartilage investigation, including conventional radiographs and ultrasound imaging. In addition to these, MR imaging holds the prime and indispensable position due to the various settings and possibilities of cartilage imaging, especially the investigation of the morphological features of cartilage, which is the crucial task for the analysis of early cartilage loss and similar disorders. The most common MR settings include T1 (longitudinal), T2 (transverse) relaxation times, and spin-echo sequences. Since individual tissues have different T1 and T2 relaxation times, that causes variations in the MR signal strength, which are observable as differences in grayscale image intensities. This fact allows for the differentiation of the healthy structure of cartilage from pathological disorders such as osteoarthritis and cartilage loss.

We use data from three variable MR sequences for the testing of the segmentation performance of cartilage modeling: proton density-weighted images, gradient echo images, and T2-weighted images. The provided testing is further based on 1500 images in total from these datasets. All the images used are from the public database, Osteoarthritis Initiative (OAI) [52]. In Figure 2, we present an example of individual datasets used in this study.

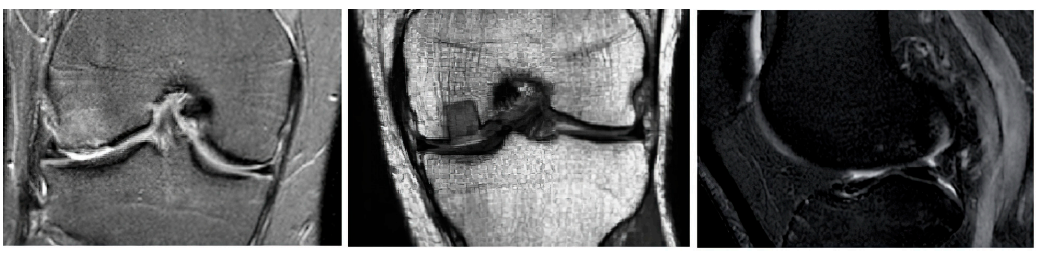

Figure 2. Examples of knee MR images used in this study, from left: T2-weighted image, proton density-weighted image, and gradient echo image.

The MR sequence based on proton density-weighted imaging is capable of recognizing the contrast between cartilage defects and abnormal cartilage composition. The further benefit of this imaging is the contrast recognition of the cartilage morphology and other tissues such as menisci and ligaments. For these reasons, this sequence is substantially important for clinical practice in the investigation of early cartilage loss, where only tiny contrast changes in the cartilage structure are notable. Thus, we mainly use the data from this sequence for the classification of cartilage loss, as we describe further. In Figure 3, we provide examples of three images of articular cartilage that contain early signs of osteoarthritis loss. This disorder is manifested as a variation of the MR signal in the form of lower image intensity in the spots (green squares) where the cartilage is missing.

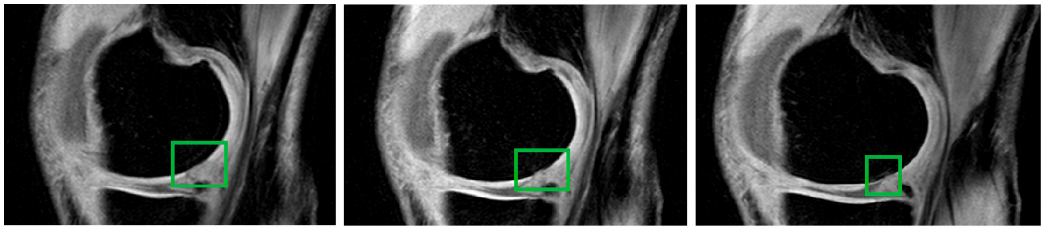

Figure 3. Examples of three images of the RoI of the articular cartilage area where cartilage is missing (green squares) as a result of the early signs of osteoarthritis.

For the purpose of our study of image segmentation, we normalized the resolution of all the MR images to provide testing under the same spatial image conditions. All the images were in format DICOM with an 8-bit bit depth. In Table 1, we provide the main acquisition parameters for individual datasets.

Table 1. Overview of acquisition parameters for individual MR imaging sequences in this study.

	Proton Density-Weighted Images	Gradient Echo Images	T2-Weighted Images
FOV (mm)	200 × 200 × 60	200 × 200 × 60	200 × 200 × 60
Matrix size	400 × 400	400 × 400	400 × 400
Acquisition time	5:30	4:50	3.40
Slice thickness (mm)	1.5	1.5	1.5
Interslice gap (mm)	0.23	0.15	0.15
Scanning mode	2D	2D	2D
Findings	Cartilage lesions	Cartilage lesions	Cartilage lesions

4.2. Segmentation Performance Analysis upon Dynamic Noise Effect

This subsection presents a comprehensive analysis of the achieved segmentation results of the proposed non-hierarchical clustering schemes. Firstly, we mention that the proposed methods are objectively compared against standard non-hierarchical clustering-based segmentation, including K-means and the FCM method, to show a comparative analysis of the segmentation performance. We first provide graphical comparisons of individual segmentation methods among each other and then the most important evolution characteristics, which evaluate the segmentation performance within gradually increasing image noise with dynamical noise intensity. To objectively compare each individual segmentation result under the noise effect, we always compare the noise-segmentation results with the segmentation for the same native image without noise influence, which is perceived as ground truth segmentation. Through this method, we construct evaluation characteristics, which report the trend of the parameters (*SSIM*, index of correlation, *MSE*, Jaccard's, and Dice coefficient), which we introduced in Section 3.7.

A constructed software testing environment enables simultaneous testing of individual segmentation methods for the single image and for a batch of MR images. To construct a segmentation analysis of dynamical noise influence, we defined a set of noise parameters that steer the noise intensity for each noise generator. Table 2 provides the noise parameter

settings that were used for all the tested MR images. For each noise generator, we used the same number of discrete steps (20) of noise intensities, which are linearly distributed.

Table 2. Noise generator settings for segmentation's performance evaluation.

Type of Noise Parameters	**Gaussian Noise** ($\sigma^2 = 0.01$, μ)	**Salt and Pepper** (d)	**Speckle Noise** (σ^2)
Noise range	0.01–0.3	0.01–0.3	0.01–0.3
Number of steps	1–20	1–20	1–20

The second issue, which was conducted for the testing, was segmentation settings for all the methods. The main parameter of all the regional segmentation methods is the number of regions (clusters), which determine the number of sets into which the spatial image is decomposed. We provide a broader analysis of five various cluster settings (3, 5, 7, 10, and 12) to show the cluster's effect on the segmentation effectivity. In the genetic algorithm, there are four steering parameters: *nSel*, *nCross*, *nMut*, and *nPop*, which have an effect on the optimized results of distributed centroids. We tried 500 random combinations of the parameters *nSel*, *nCross*, and *nMut* to be used for the optimization. For each variant, we evaluated the fitness function of the best candidate solution. Finally, we selected the following combination (Table 3) that is used in this study, where we experimentally achieved the highest fitness for the mentioned steering parameters.

Table 3. Parameter settings for the genetic algorithm of clustering optimization.

Parameter	***nSel***	***nCross***	***nMut***	***nPop***
	20% of (p)	30% of (p)	28% of (p)	$\{20,\ 50,\ 100, 150,\ 200\}$

For all the parameters, we used single-value settings as the percentual ratio of the population size (p) to be used for the clustering-based segmentation apart from the number of populations (*nPop*), where we tested and reported various settings for the segmentation performance analysis.

A similar analysis we performed for PSO-based clustering optimization. Here, we tested various settings of swarm size (*nSwarm*), which is the same as the population size (p). The next parameter is the neighborhood size (*nNeighbor*), which determines the size of the extent of social interactions within the swarm. For the parameter number of iterations (*nIter*), we used the same settings as for the (*nPop*). Lastly, we mention the acceleration coefficients ($c_1,\ c_2$), which control the stochastic influence of the cognitive and social components on the overall velocity of a particle. Table 4 provides the settings for the parameters for PSO-based optimization.

Table 4. Parameter settings for PSO for clustering optimization.

Parameter	***nNeighbor***	***nIter***	c_1, c_2
	5% of (*nSwarm*)	$\{20,\ 50,\ 100, 150,\ 200\}$	$\{2.5,\ 0.5\}$

Note that we used the same settings for both optimization strategies for the number of populations (*nPop*) and the number of iterations (*nIter*) for both optimizations to be comparable to each other. Additionally, the size of the population (p) and swarm (*nSwarm*) are set to the value 500 for both cases of optimization.

Furthermore, we introduce the graphical comparisons (Figures 4–6) of the noise influence on segmentation performance. As we outlined earlier, we designed the analysis, which evaluates the dynamical effect of the noise influence on the segmentation performance. For this purpose, we used three noise generators: Gaussian, Speckle, and Salt and Pepper noise with variable intensity.

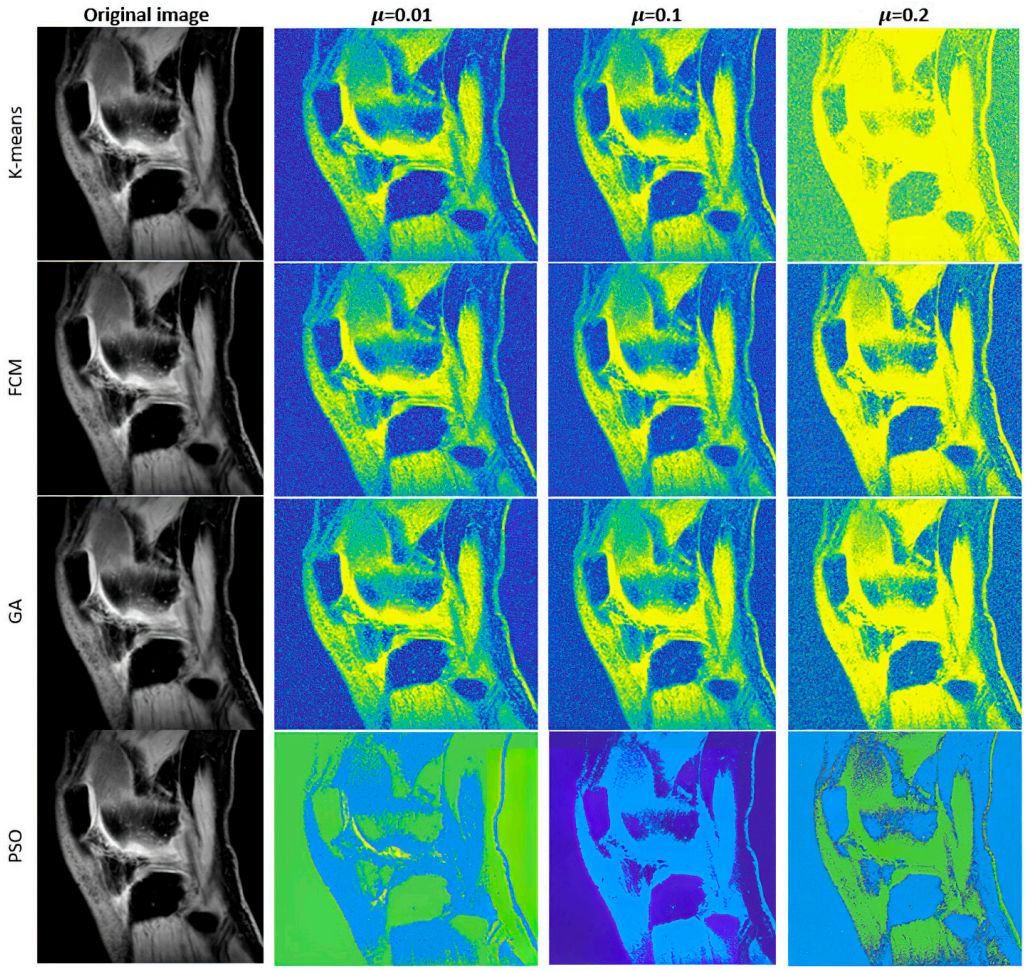

Figure 4. Examples of multiregional segmentation maps for optimized clustering schemes with a genetic algorithm (*GA*) and a PSO with K-means and FCM-based clustering for 4 regions where segmentation is influenced by Gaussian noise with 3 various intensity levels: $\sigma^2 = 0.01$, $\mu = \{0.01,\ 0.1,\ 0.2\}$.

Judging by a visual comparison of individual noise generators, the higher the applied noise intensity, the higher the influence on segmentation performance. Nevertheless, just based on the visual comparison, the differences among individual noise types are notable. Significant differences are notable between Speckle and Gaussian noise on the one side and Salt and Pepper noise on the other side, where noise has a higher impact on the segmentation performance. This is caused by the impulse character of the noise, which worsens segmentation performance.

The main aim of this analysis is to provide an objective comparison of the segmentation performance under gradual noise influence. To perform such analysis, we constructed evolution trend characteristics, which report the development of the segmentation performance of the proposed optimized clustering schemes in contrast with conventional clustering techniques. All the presented trends are the results of averaging the results for the entire MR dataset, which contains 1500 images. Firstly, we provide the comparison of genetic algorithm-based optimization for Gaussian noise with the $nPop = 200$ and the same settings for PSO ($nIter = 200$) under Salt and Pepper noise (Figures 7 and 8).

Based on the comparisons, the proposed optimized schemes show mostly better results when compared with the conventional algorithms. Just in the case of the correlation trend (Figure 7), FCM gives the best results, and in the case of the Jaccard coefficient for PSO (Figure 8), there are only small differences between PSO and FCM. Nevertheless, in total, the optimized schemes provide promising stable segmentation results under various noise influences. Generally, the optimized schemes are significantly better than K-means and

comparably better than FCM, which is, on the other hand, better than K-means, which was predictable.

Any concept of multiregional segmentation is always linked with the number of segmentation regions (clusters) into which the original spatial image area is decomposed. Therefore, one of the important aspects of segmentation performance is the study of the effect of various numbers of clusters on segmentation performance. For this reason, we provide the analysis of Gaussian noise for genetic algorithm-based clustering (Figure 9) and Salt and Pepper analysis for PSO-based clustering (Figure 10). Both analyses were performed for the same number of clusters: {3, 5, 7, 10, and 12}.

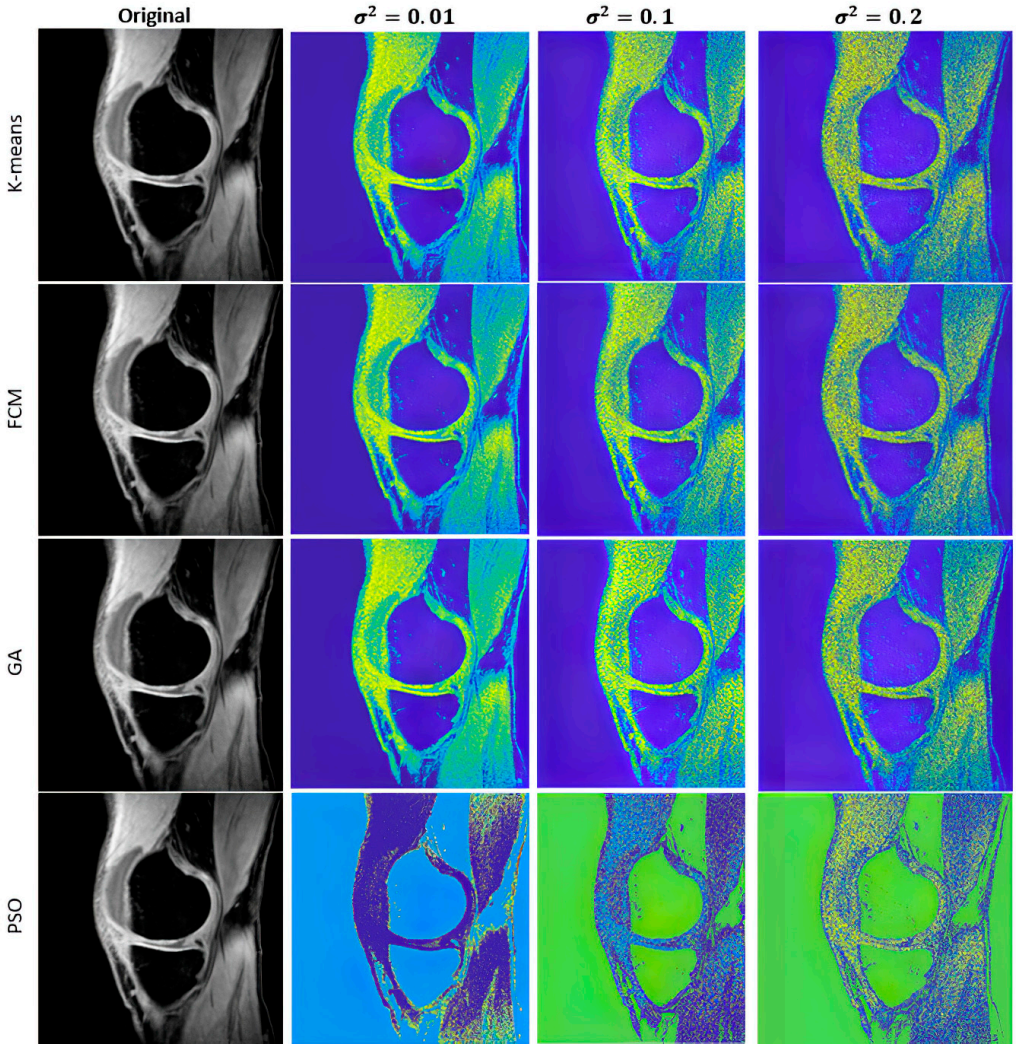

Figure 5. Examples of multiregional segmentation maps for optimized clustering schemes with a genetic algorithm (*GA*) and a PSO with K-means and FCM-based clustering for 4 regions where segmentation is influenced by Speckle noise with 3 various intensity levels: $\sigma^2 = \{0.01,\ 0.1,\ 0.2\}$.

The results show various segmentation performances for both types of dynamical noise influence for individual segmentation techniques. Judging by the results, more significant variations are notable for the genetic algorithm in PSO, especially in *SSIM* and Jaccard-based evaluation, where individual results are mostly overlayed. Generally, it can be concluded that the fewer clusters selected, the worse segmentation performance is achieved, with the exception of the Jaccard coefficient in *GA* clustering and *MSE* for both optimizations.

The last trend characteristics (Figure 11), which we provide, are focused on the effect of various numbers of populations (*GA*) and iterations (PSO) on the segmentation

performance. Here, we are focused on the analysis of structural similarity (*SSIM*) under Speckle noise with various noise intensities against K-means (red trend) and FCM (blue trend). As the results show, conventional methods have much worse structural similarity when compared with all settings of optimization techniques. On the other hand, we did not achieve more significant differences between individual settings of populations and iterations. Thus, we can conclude that these parameters do not have a significant influence on the segmentation performance seen in the stability in various image conditions.

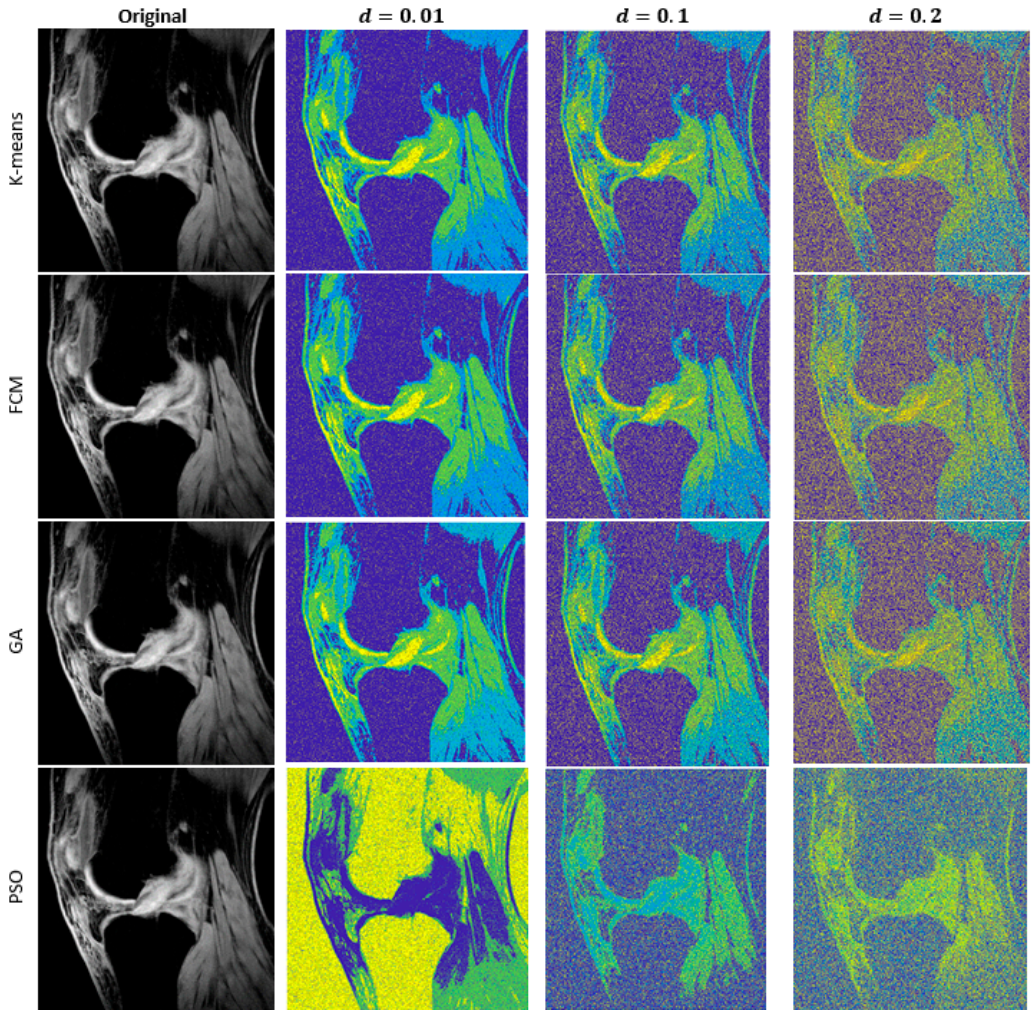

Figure 6. Examples of multiregional segmentation maps for optimized clustering schemes with a genetic algorithm (*GA*) and a PSO with K-means and FCM-based clustering for 4 regions where segmentation is influenced by Salt and Pepper noise with 3 various intensity levels: $d = \{0.01, 0.1, 0.2\}$.

Lastly, we provide a statistical comparison (Table 5) of median values for individual methods for all the types of noise and their intensities together to quantify the aforementioned trends by their average values, which is better for the global comparison of individual methods among each other. Here, we compare individual settings of the number of clusters from the perspective of their median values. We highlighted the best results for each parameter by bolt with a green mark; contrarily, the worst results are indicated by a red mark. As it is obvious from Table 5, apart from the correlation coefficient, the best results are indicated for genetic algorithm-based clustering, which can be, from this perspective, perceived as the best alternative, outperforming the other methods.

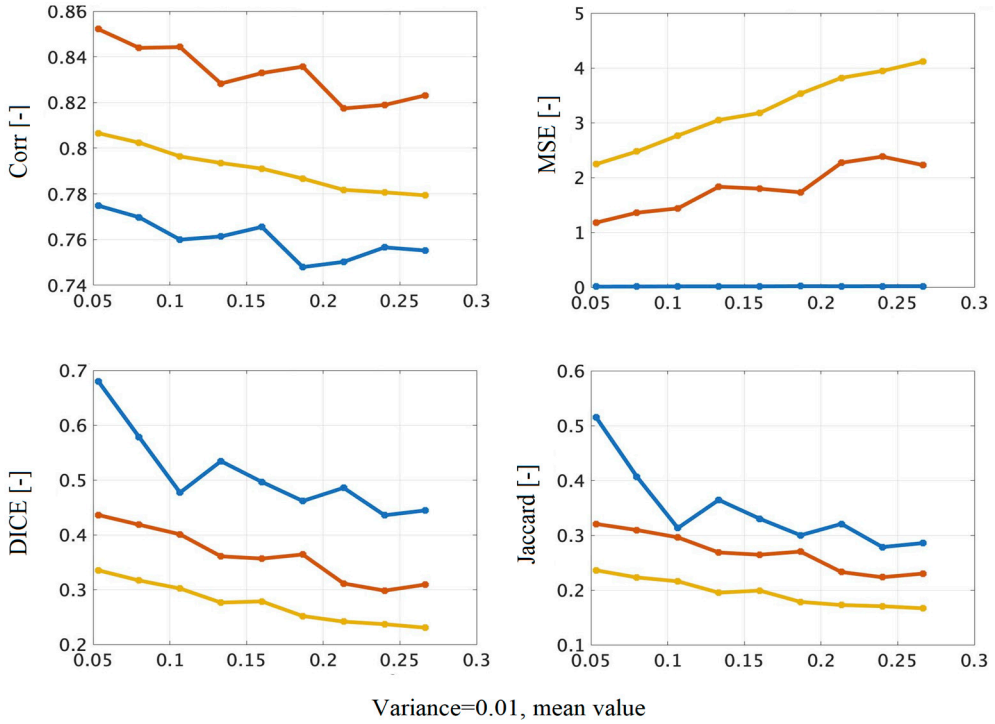

Figure 7. Trend characteristics for segmentation performance evaluation based upon Gaussian noise with dynamic noise intensity. Segmentation is computed for 7 clusters: the yellow trend represents K-means, the red FCM, and the blue proposed clustering with a *GA* optimization with 200 populations.

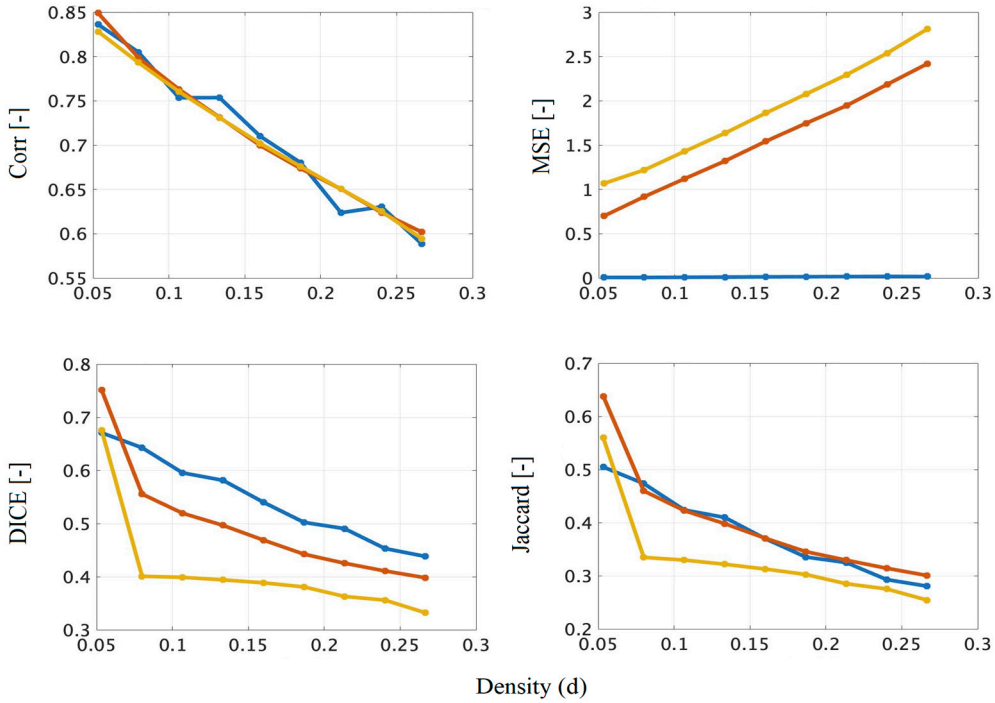

Figure 8. Trend characteristics for segmentation performance evaluation based upon Salt and Pepper noise with dynamic noise intensity. Segmentation is computed for 7 clusters: the yellow trend represents K-means, the red FCM, and the blue proposed clustering with a PSO optimization with 200 iterations.

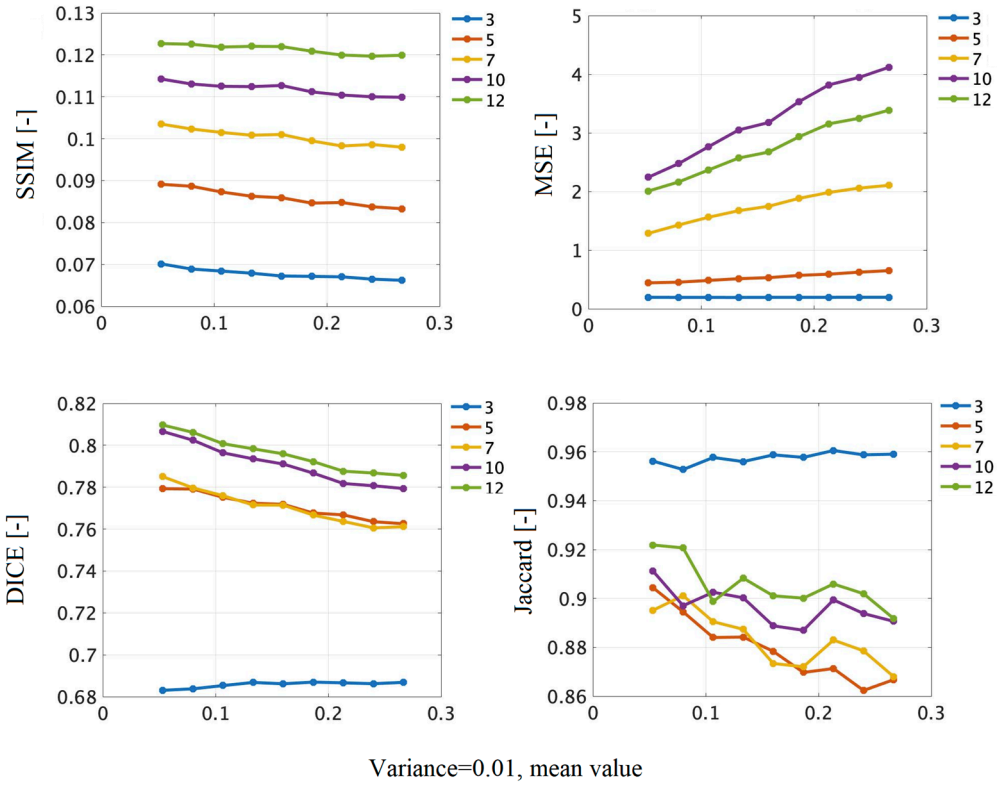

Figure 9. Trend characteristics for the segmentation performance of GA-based clustering with 200 populations upon Gaussian noise with dynamic noise intensity. Segmentation is computed for {3, 5, 7, 10, and 12} clusters.

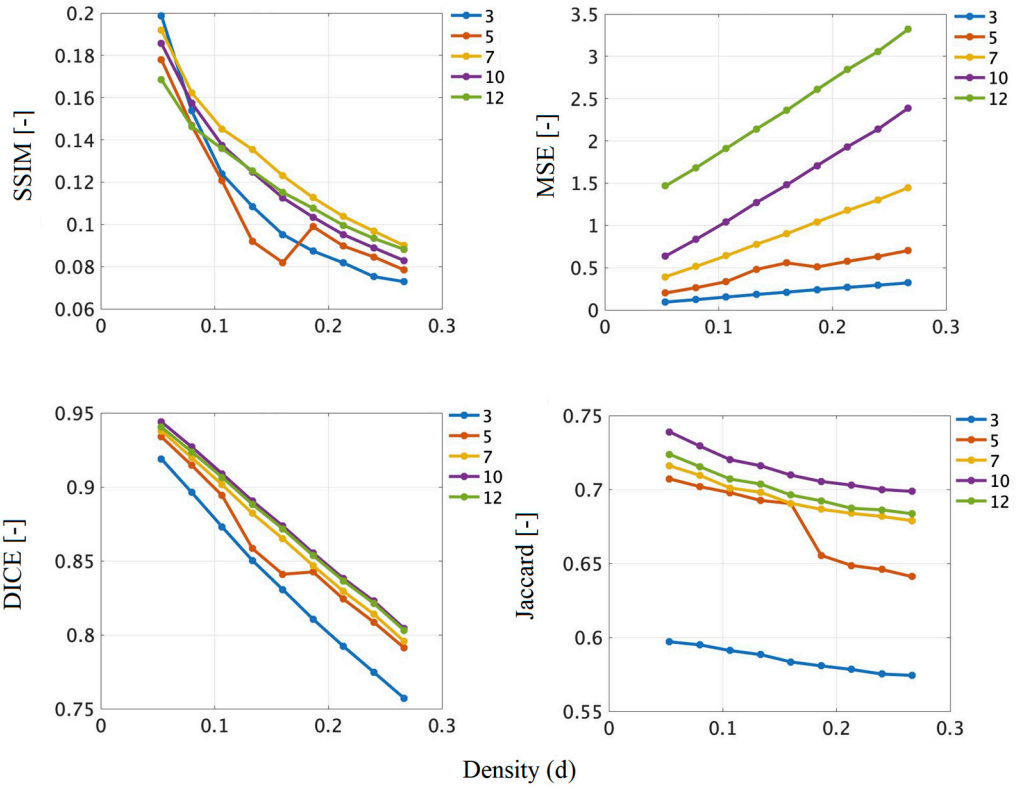

Figure 10. Trend characteristics for the segmentation performance of PSO-based clustering with 200 iterations upon Salt and Pepper noise with dynamic noise intensity. Segmentation is computed for {3, 5, 7, 10, and 12} clusters.

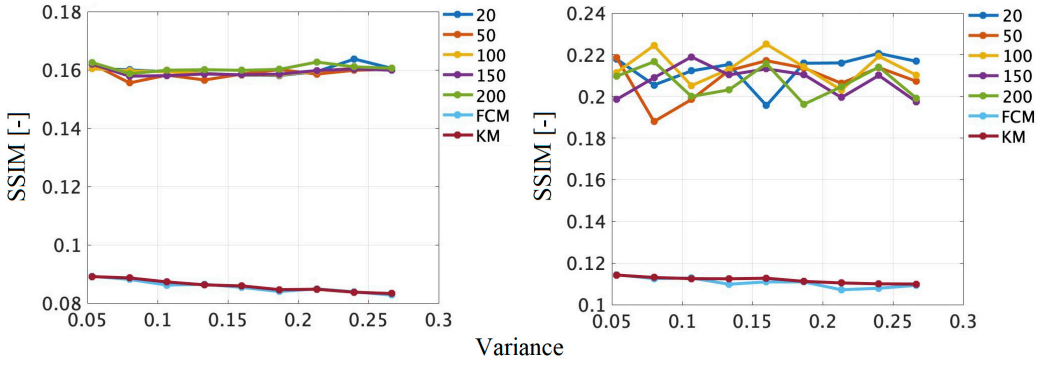

Figure 11. Comparative analysis of Speckle noise influence on various setting populations of GA-based clustering (**left**) and iterations of PSO (**right**) with K-means and PSO based on the analysis of SSIM.

Table 5. Statistical analysis (median values) of performance evaluation for all the noise generators.

Method	Number of Clusters	Corr [-]	DICE [-]	Jaccard [-]	SSIM [-]	MSE [-]
GA	3	0.7300	**0.7766**	**0.6423**	0.2322	0.0165
	5	0.7600	0.5019	0.3589	0.2428	0.0131
	7	0.7800	0.5362	0.3897	0.2679	0.0151
	10	0.7800	0.5593	0.4114	0.2898	**0.0130**
	12	0.7900	0.4517	0.3230	**0.3021**	0.0159
PSO	3	0.7400	0.7451	0.6149	0.2125	0.0211
	5	0.7500	0.4821	0.3281	0.2316	0.0332
	7	0.7400	0.5260	0.3897	0.2541	0.0344
	10	0.7700	0.5391	0.4022	0.2655	0.0351
	12	0.7700	0.4122	0.4221	0.2911	0.0159
FCM	3	0.7300	0.6266	0.5283	0.1771	0.2699
	5	0.8100	0.6592	0.5503	0.1912	0.3781
	7	0.8300	0.4205	0.3372	0.1996	0.9469
	10	0.8500	0.4254	0.3415	0.2022	1.6206
	12	**0.8600**	0.3564	0.2862	0.2111	2.1645
K-means	3	**0.7200**	0.7530	0.5254	**0.1609**	0.1763
	5	0.7900	0.6268	0.5179	0.1774	0.4866
	7	0.7900	0.3005	0.2303	0.1903	1.5730
	10	0.8100	0.3469	0.2757	0.2006	**2.9123**
	12	0.8200	**0.2648**	**0.1987**	0.2092	2.4504

The last characteristic, which we publish in this section, is focused on the time complexity of the clustering-based algorithm. The robustness, which we introduced earlier, shows important segmentation performance as the proposed segmentation schemes outperform conventional algorithms. On the other hand, the important feature of each segmentation algorithm is also the computing time required for making the segmentation model. Here, we show the comparisons of the proposed schemes against the conventional clustering methods. All the tests were conducted on the following PC configuration: Intel(R) Core(TM) i5-10300H CPU@2.50 GHz, RAM: 16.0 GB. Note that the time results represent the total time for batch segmentation of 500 MR images.

The results of the time complexity show significant differences between the conventional algorithms (Table 6) and the proposed optimized clustering schemes (Table 7). While the conventional algorithms achieve the computing time in seconds, the optimized schemes achieve it in minutes, which is comparable to worse results. These differences are surely explained by the optimization strategies, which require a longer time to compute the segmentation model.

Table 6. Computing costs in seconds of clustering methods K-means and FCM.

Algorithm	**K-Means**					**FCM**				
Clusters	3	5	7	10	12	3	5	7	10	12
Gauss	15.45	18.24	22.34	28.38	35.41	96.56	104.54	107.21	110.68	112.43
SaP	15.96	16.17	19.35	20.35	32.98	97.58	100.28	100.47	101.21	102.65
Speckle	15.22	16.40	19.73	23.41	31.32	96.82	97.06	100.15	101.45	103.27

Table 7. Computing costs in minutes of the proposed clustering methods based on the *GA* and PSO for 200 populations.

Algorithm	***GA***					**PSO**				
Clusters	20	50	100	150	200	20	50	100	150	200
Gauss	6	9	14	17	23	4	9	12	15	21
SaP	5	9	15	17	23	4	8	15	16	21
Speckle	5	8	13	19	25	3	7	13	19	23

4.3. Early Signs of Articular Cartilage Classification

This section brings the most interesting results for the clinical evaluation of articular cartilage as a classification of early signs of osteoarthritis, which manifest as cartilage loss. This is substantially important to distinguish these cartilage features from those of healthy cartilage with compact structure, which is usually represented by a homogenous MR signal. On the other hand, cartilage loss is standardly represented by intensity variations and a weaker MR signal when compared with healthy cartilage (Figure 12). In order to classify such early signs of cartilage loss from the healthy cartilage structure, we used two convolutional neural networks (CNNs): *GoogLeNet* and *ResNet 18*, with various hyperparameter settings to find the best alternative for the cartilage loss classification. For this classification, we used the segmentation data of articular cartilage based on the proposed clustering scheme with a genetic algorithm. This alternative is used due to its best performance, as we declared in the previous section. We performed segmentation for 1000 MR images in total, which were equally divided into 500 healthy images and 500 images with early cartilage loss. As an example of the segmentation based on the genetic algorithm-based clustering, we show the closed segmentation curve, which outlines a part of the cartilage area (healthy cartilage) where other parts of the segmentation model are eliminated.

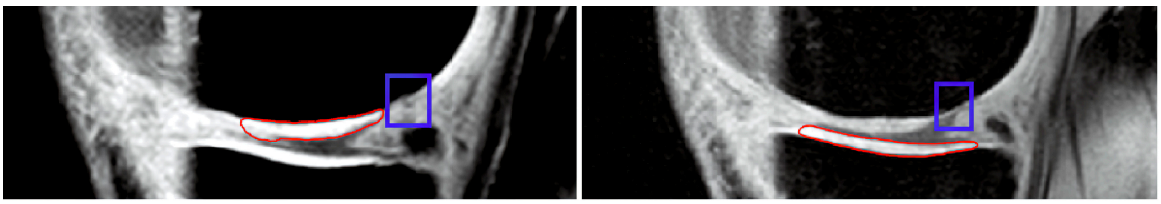

Figure 12. Examples of detection tibial (**left**) and femoral (**right**) articular cartilage by GA-based clustering, where the blue squares indicate the spots of early cartilage loss.

We built the classification analysis based on the segmentation results, which we present in Figure 12. We selected two types of convolutional neural networks, GoogLeNet and ResNet 18, to show a comparative analysis of the classification performance to recognize early cartilage loss. We studied the classification performance within various hyperparameter settings, including various number of epochs and the ratio of the training/validation dataset. The tested hyperparameters are summarized in Table 8. We used the same parameters for both CNNs to achieve comparable results. The entire classification procedure for the recognition of cartilage loss is depicted in Figure 13.

Table 8. Hyperparameter settings for the classification of cartilage loss.

Parameter	Settings
Number of epochs	{5, 10, 20, 30, 50}
Learning rate	0.0001
Training/validation ratio	{0.4, 0.6, 0.8}
Validation frequency	10

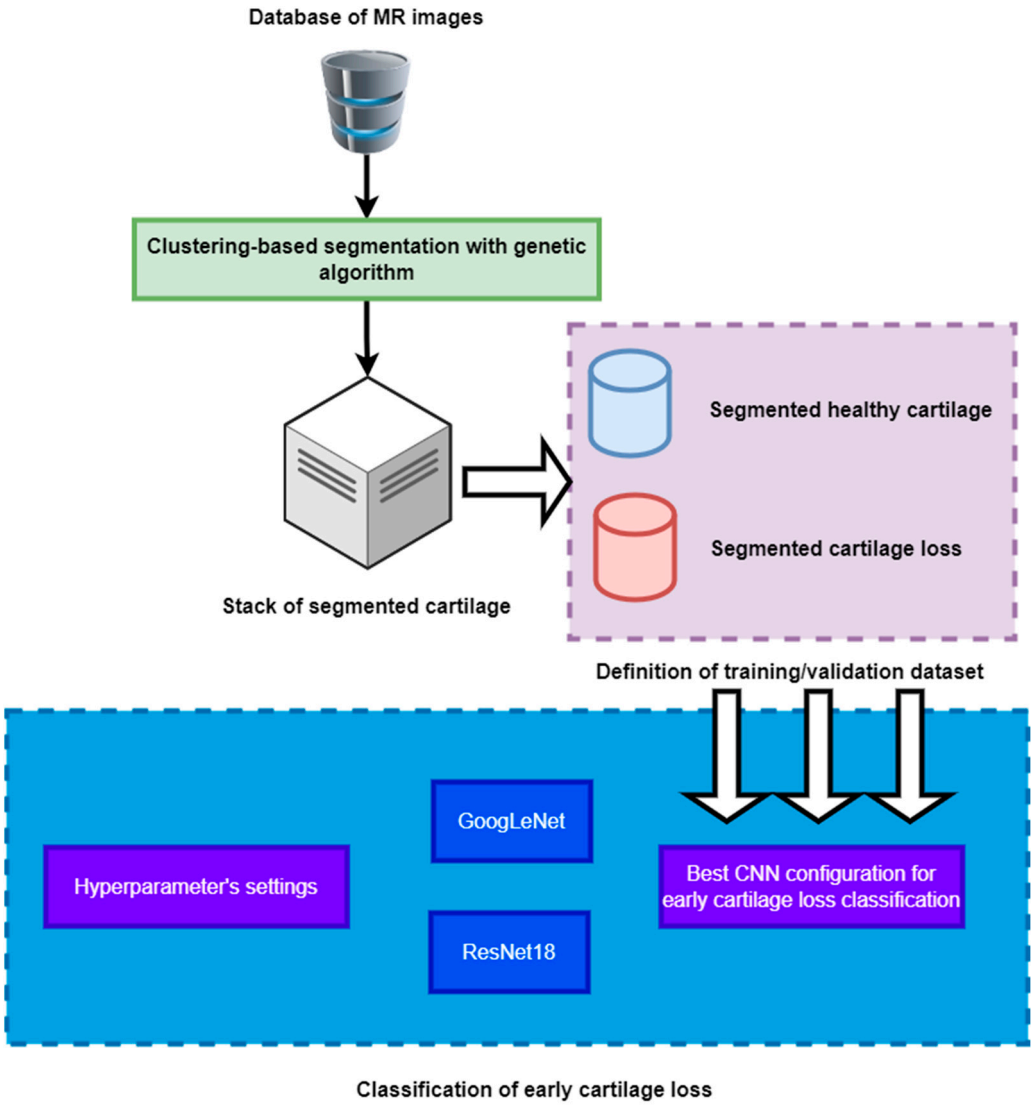

Figure 13. Flowchart of the whole classification design for early cartilage loss classification based on the segmentation data from genetic algorithm-based clustering.

We present the results (Table 9) of comparative analysis of the classification of early cartilage loss from the healthy cartilage to recognize degenerative changes in the cartilage structure based on clustering with a genetic algorithm. We provide testing of both CNNs for various numbers of epochs and the other hyperparameters, which are stated in Table 8. We present these results for the training/validation ratio of 0.8, where we achieved the best classification results from the other alternatives. The classification performance is evaluated based on the three parameters, including accuracy (*Acc*), sensitivity (*Se*), and specificity (*Sp*). Judging by the accuracy, the best settings of CNN were achieved for ResNet 18 (99.92%), but with less significant differences than other settings.

Table 9. Evaluation of CNN performance for various settings, where the best results are indicated in green, while the worst are indicated in red.

Epochs	*CNN*	*Acc*	*Se*	*Sp*
5	Resnet 18	**99.92%**	98.15%	97.12%
	GoogleNet	97.83%	95.45%	94.36%
10	ResNet 18	99.75%	**99.75%**	95.14%
	GoogleNet	95.50%	91.77%	92.48%
20	ResNet 18	99.75%	96.54%	94.74%
	GoogleNet	96.75%	**89.47%**	**92.44%**
30	ResNet 18	**99.92%**	97.48%	**97.45%**
	GoogleNet	**98.83%**	**97.74%**	92.56%

5. Conclusions and Discussion

MR image segmentation of musculoskeletal images plays a crucial role in clinical analysis to objectively identify and recognize various disorders such as cartilage loss, which may significantly impair movement abilities. There are variable segmentation strategies based on edge detection, active curves, histogram thresholding, and others that may be adopted for this task, as various studies report, for instance. In addition to these studies, non-hierarchical clustering plays an indispensable role, as we report in this study, in generating a multiregional model with the consequent possibility to extract cartilage features and recognize early cartilage loss [53–55].

Since one of the main drawbacks of the conventional clustering methods (K-means and FCM) is a manual selection of initial centroids and the clustering, respective segmentation performance is influenced by this selection. Our research is focused in the area of automatic and reliable placement, the initial centroids, and making the initial clusters of pixels based on the evolutionary computing strategies, including genetic algorithms and PSO. These optimization tools enable consecutive breeding and selection of the most suitable combination of the centroids based on the fitness function, reflecting entropy and statistical features of individual clusters to find the segmentation regions with homogenous pixel features distribution.

In this study, we provide various testing of steering the parameters of evolutionary methods to demonstrate their influence on segmentation performance. We reported on various performance tests where we studied the segmentation performance under the dynamic influence of various noises with variable intensities. Based on such tests, we mainly objectively achieved that the genetic algorithm-based clustering mostly outperformed PSO and also the conventional methods, which have been considered for a long time as standard non-hierarchical clustering strategies. On the other hand, we objectively point out certain limitations of evolutionary-based clustering. Mainly, it is the computing time, especially when processing a batch of MR images, where the conventional strategies achieved the computing time in seconds while the proposed optimized methods did so in minutes, which may be considered a significant difference. Thus, it is obvious that better segmentation performance is linked with higher computing costs.

The most important clinical application of the regional segmentation of the proposed strategies is it is a recognition of early cartilage loss, which may have severe consequences on the musculoskeletal system when left untreated. Therefore, we suggest using multiregional segmentation based on the proposed genetic algorithm optimization to classify healthy cartilage from early cartilage loss. Based on the comparative analysis of CNNs, *GoogLeNet* and *ResNet 18*, we show a relatively high performance of 99.92% for the best hyperparameter settings.

This analysis showed the performance for MR image segmentation of the knee area based on modern optimization evolutionary computing in contrast with conventional methods. It also showed the classification performance, which was based on the segmentation results. On the other hand, there are some open issues for future research. We are going to focus on testing evolutionary algorithms on further different sequences for

cartilage imaging to show a comparative performance of optimized clustering for various MR data structures. The second issue will be an objective analysis of the segmentation performance with a maximally reduced number of the iterations (populations) to achieve the segmentation model with acceptable performance due to a negative influence of these parameters on the computing time. Lastly, fewer clusters also negatively influence segmentation performance; therefore, it creates the issue of finding the segmentation model of articular cartilage with an ideally higher number of clusters.

Author Contributions: Conceptualization, J.K., M.C. and A.V.; methodology, M.C. and D.O.; software, A.V., J.S. and D.O.; validation, J.K., M.P. and D.O.; formal analysis, J.K. and J.S.; investigation, A.V. and J.S.; resources, M.P.; data curation, A.V.; writing—original draft preparation, J.K. and A.V.; writing—review and editing, M.A. and J.K.; visualization, M.A.; supervision, M.A., M.C. and A.V.; project administration, M.P.; funding acquisition, M.P. All authors have read and agreed to the published version of the manuscript.

Funding: This paper was supported by project No. CZ.02.1.01/0.0/0.0/17 049/0008441, Innovative Therapeutic Methods of Musculoskeletal System in Accident Surgery within the Operational Programme Research, Development, and Education financed by the European Union and by the state budget of the Czech Republic. The work and the contributions were supported by the project SV4502261/SP2022/98 "Biomedical Engineering systems XVIII". This publication has been produced with the support of the Integrated Infrastructure Operational Program for the project: Systemic Public Research Infrastructure—Biobank for Cancer and Rare diseases, ITMS: 313011AFG5, co-financed by the European Regional Development Fund.

Data Availability Statement: Data are used from the publicly open clinical database *The Osteoarthritis Initiative*.

Conflicts of Interest: The authors declare no conflict of interest.

References

1. Yang, Y.; Guo, Y.; Yu, S.; Zou, B. Computed tomography and magnetic resonance imaging findings in gouty arthritis involving large joints of the upper extremities. *BMC Med. Imaging* **2022**, *22*, 167. [CrossRef]
2. Fan, T.; Chen, S.; Zeng, M.; Li, J.; Wang, X.; Ruan, G.; Cao, P.; Zhang, Y.; Chen, T.; Ou, Q.; et al. Osteophytes mediate the associations between cartilage morphology and changes in knee symptoms in patients with knee osteoarthritis. *Arthritis Res. Ther.* **2022**, *24*, 217. [CrossRef] [PubMed]
3. Gobbi, A.; Lane, J.G.; Morales, M.; D'Ambrosi, R. Articular cartilage delamination at eight years following cellular-based repair procedures: A case reports. *J. Exp. Orthop.* **2022**, *9*, 90. [CrossRef] [PubMed]
4. Katagiri, H.; Takahashi, M.; Murata, H.; Wasa, J.; Miyagi, M.; Honda, Y. Direct femoral head approach without surgical dislocation for femoral head chondroblastoma: A report of two cases. *BMC Surg.* **2022**, *22*, 327. [CrossRef] [PubMed]
5. Hänninen, N.E.; Liimatainen, T.; Hanni, M.; Gröhn, O.; Nieminen, M.T.; Nissi, M.J. Relaxation anisotropy of quantitative MRI parameters in biological tissues. *Sci. Rep.* **2022**, *12*, 12155. [CrossRef]
6. Schneider, M.T.-Y.; Rooks, N.; Besier, T. Cartilage thickness and bone shape variations as a function of sex, height, body mass, and age in young adult knees. *Sci. Rep.* **2022**, *12*, 11707. [CrossRef] [PubMed]
7. Li, J.; Wang, Y.; Wei, Y.; Kong, D.; Lin, Y.; Wang, D.; Cheng, S.; Yin, P.; Wei, M. The effect of talus osteochondral defects of different area size on ankle joint stability: A finite element analysis. *BMC Musculoskelet. Disord.* **2022**, *23*, 500. [CrossRef]
8. Hoey, S.; O'Sullivan, J.; Byrne, J.; Devine, S.; Toomey, W.; McAllister, H.; Skelly, C. Ultrasound screening protocol for osteochondrosis at selected predilection sites in thoroughbred yearlings. *Ir. Vet. J.* **2022**, *75*, 8. [CrossRef] [PubMed]
9. Olivier, T.; Kasprzak, K.; Herteleer, M.; Demondion, X.; Jacques, T.; Cotten, A. Anatomical study of the sternoclavicular joint using high-frequency ultrasound. *Insights Into Imaging* **2022**, *13*, 66. [CrossRef]
10. Sun, T.-Y.; Hsu, C.-L.; Tseng, W.-C.; Yeh, T.-T.; Huang, G.-S.; Shen, P.-H. Risk Factors Associated with Cartilage Defects after Anterior Cruciate Ligament Rupture in Military Draftees. *J. Pers. Med.* **2022**, *12*, 1076. [CrossRef]
11. Awan, M.J.; Rahim, M.S.M.; Salim, N.; Rehman, A.; Nobanee, H.; Shabir, H. Improved Deep Convolutional Neural Network to Classify Osteoarthritis from Anterior Cruciate Ligament Tear Using Magnetic Resonance Imaging. *J. Pers. Med.* **2021**, *11*, 1163. [CrossRef]
12. Laborde, C.M.; Castro-Santos, P.; Díaz-Peña, R. Contribution of Multiplex Immunoassays to Rheumatoid Arthritis Management: From Biomarker Discovery to Personalized Medicine. *J. Pers. Med.* **2020**, *10*, 202. [CrossRef]
13. Xiangyu, D.; Huan, Z.; Yahan, Y. Ultrasonic Image Segmentation Algorithm of Thyroid Nodules Based on DPCNN. *Lect. Notes Electr. Eng.* **2022**, *784*, 163–174. [CrossRef]
14. Ferre, L.S.; Di Nisio, F.G.; Mendonça, C.J.A.; Belo, I.M. Comparative analysis of tibial plateau fracture osteosynthesis: A finite element study. *J. Mech. Behav. Biomed. Mater.* **2022**, *134*, 105392. [CrossRef]

15. Armstrong, A.; Bhave, S.; Buko, E.; Chase, K.; Tóth, F.; Carlson, C.; Ellermann, J.; Kim, H.; Johnson, C. Quantitative T2 and T1ρ mapping are sensitive to ischemic injury to the epiphyseal cartilage in an in vivo piglet model of Legg-Calvé-Perthes disease. *Osteoarthr. Cartil.* **2022**, *30*, 1244–1253. [CrossRef] [PubMed]
16. Sifre, V.; Ten-Esteve, A.; Serra, C.I.; Soler, C.; Alberich-Bayarri, Á.; Segarra, S.; Martí-Bonmatí, L. Knee Cartilage and Subchondral Bone Evaluations by Magnetic Resonance Imaging Correlate with Histological Biomarkers in an Osteoarthritis Rabbit Model. *Cartilage* **2022**, *13*, 19476035221118166. [CrossRef] [PubMed]
17. Khan, S.; Azam, B.; Yao, Y.; Chen, W. Deep collaborative network with alpha matte for precise knee tissue segmentation from MRI. *Comput. Methods Programs Biomed.* **2022**, *222*, 106963. [CrossRef] [PubMed]
18. Mastbergen, S.; Ooms, A.; Turmezei, T.; MacKay, J.; Van Heerwaarden, R.; Spruijt, S.; Lafeber, F.; Jansen, M. Subchondral bone changes after joint distraction treatment for end stage knee osteoarthritis. *Osteoarthr. Cartil.* **2022**, *30*, 965–972. [CrossRef]
19. Liu, L.; Liu, H.; Zhen, Z.; Zheng, Y.; Zhou, X.; Raithel, E.; Du, J.; Hu, Y.; Chen, W.; Hu, X. Analysis of Knee Joint Injury Caused by Physical Training of Freshmen Students Based on 3T MRI and Automatic Cartilage Segmentation Technology: A Prospective Study. *Front. Endocrinol.* **2022**, *13*, 839112. [CrossRef]
20. Yang, C.-M.; Liu, Y.; Wang, Y.-T.; Li, Y.-P.; Hou, W.-H.; Duan, S.; Wang, J.-Q. A Novel Adaptive Kernel Picture Fuzzy C-Means Clustering Algorithm Based on Grey Wolf Optimizer Algorithm. *Symmetry* **2022**, *14*, 1442. [CrossRef]
21. Kim, K.B.; Song, D.H.; Park, H.J. Robust Automatic Segmentation of Inflamed Appendix from Ultrasonography with Double-Layered Outlier Rejection Fuzzy C-Means Clustering. *Appl. Sci.* **2022**, *12*, 5753. [CrossRef]
22. Zhu, J.; Wang, F.; You, H. SAR Image Segmentation by Efficient Fuzzy C-Means Framework with Adaptive Generalized Likelihood Ratio Nonlocal Spatial Information Embedded. *Remote Sens.* **2022**, *14*, 1621. [CrossRef]
23. Kim, K.B.; Song, D.H.; Park, H.J. Intelligent Automatic Segmentation of Wrist Ganglion Cysts Using DBSCAN and Fuzzy C-Means. *Diagnostics* **2021**, *11*, 2329. [CrossRef] [PubMed]
24. Takeuchi, R.D.O.A.; Ulbricht, L.; Magrin, F.G.S.; Ganacim, F.I.S.; Fernandes, L.G.; Romaneli, E.F.R.; Junior, J.U. Comparison of Traditional Image Segmentation Methods Applied to Thermograms of Power Substation Equipment. *Energies* **2022**, *15*, 7477. [CrossRef]
25. Kumar, S.V.A.; Yaghoubi, E.; Proença, H. A Fuzzy Consensus Clustering Algorithm for MRI Brain Tissue Segmentation. *Appl. Sci.* **2022**, *12*, 7385. [CrossRef]
26. Tabianan, K.; Velu, S.; Ravi, V. K-Means Clustering Approach for Intelligent Customer Segmentation Using Customer Purchase Behavior Data. *Sustainability* **2022**, *14*, 7243. [CrossRef]
27. Zhang, P.; Zhang, R.X.; Chen, X.S.; Zhou, X.Y.; Raithel, E.; Cui, J.L.; Zhao, J. Clinical validation of the use of prototype software for automatic cartilage segmentation to quantify knee cartilage in volunteers. *BMC Musculoskelet. Disord.* **2022**, *23*, 19. [CrossRef]
28. Ruckli, A.C.; Schmaranzer, F.; Meier, M.K.; Lerch, T.D.; Steppacher, S.D.; Tannast, M.; Zeng, G.; Burger, J.; Siebenrock, K.A.; Gerber, N.; et al. Automated quantification of cartilage quality for hip treatment decision support. *Int. J. Comput. Assist. Radiol. Surg.* **2022**, *17*, 2011–2021. [CrossRef]
29. Peiffer, M.; Burssens, A.; Duquesne, K.; Last, M.; De Mits, S.; Victor, J.; Audenaert, E. Personalised statistical modelling of soft tissue structures in the ankle. *Comput. Methods Programs Biomed.* **2022**, *218*, 106701. [CrossRef]
30. Harkey, M.S.; Michel, N.; Kuenze, C.; Fajardo, R.; Salzler, M.; Driban, J.B.; Hacihaliloglu, I. Validating a Semi-Automated Technique for Segmenting Femoral Articular Cartilage on Ultrasound Images. *Cartilage* **2022**, *13*, 19476035221093069. [CrossRef]
31. Ebrahimkhani, S.; Dharmaratne, A.; Jaward, M.H.; Wang, Y.; Cicuttini, F.M. Automated segmentation of knee articular cartilage: Joint deep and hand-crafted learning-based framework using diffeomorphic mapping. *Neurocomputing* **2022**, *467*, 36–55. [CrossRef]
32. Song, K.; Kosik, K.B.; Gribble, P.A.; Wikstrom, E.A. Reliability of Manually Segmenting T1ρ Magnetic Resonance Sequences of Talar Articular Cartilage. *J. Sport Rehabil.* **2022**, *31*, 111–114. [CrossRef] [PubMed]
33. Tang, X.; Guo, D.; Liu, A.; Wu, D.; Liu, J.; Xu, N.; Qin, Y. Fully Automatic Knee Joint Segmentation and Quantitative Analysis for Osteoarthritis from Magnetic Resonance (MR) Images Using a Deep Learning Model. *Med. Sci. Monit.* **2022**, *28*, e936733-1. [CrossRef] [PubMed]
34. Swamy, M.S.M.; Holi, M.S. Segmentation, visualization and quantification of knee joint articular cartilage using MR images. *Lect. Notes Electr. Eng.* **2013**, *213*, 321–332. [CrossRef]
35. Panfilov, E.; Tiulpin, A.; Klein, S.; Nieminen, M.T.; Saarakkala, S. Improving robustness of deep learning based knee mri segmentation: Mixup and adversarial domain adaptation. In Proceedings of the 2019 IEEE/CVF International Conference on Computer Vision Workshops, ICCV Workshops 2019, Seoul, Republic of Korea, 27–28 October 2019; pp. 450–459. [CrossRef]
36. Pröve, P.-L.; Well, E.J.-V.; Stanczus, B.; Morlock, M.M.; Herrmann, J.; Groth, M.; Säring, D.; der Mauer, M.A. Automated segmentation of the knee for age assessment in 3D MR images using convolutional neural networks. *Int. J. Leg. Med.* **2019**, *133*, 1191–1205. [CrossRef]
37. Schmaranzer, F.; Helfenstein, R.; Zeng, G.; Lerch, T.; Novais, E.N.; Wylie, J.D.; Kim, Y.-J.; Siebenrock, K.A.; Tannast, M.; Zheng, G. Automatic MRI-based Three-dimensional Models of Hip Cartilage Provide Improved Morphologic and Biochemical Analysis. *Clin. Orthop. Relat. Res.* **2019**, *477*, 1036–1052. [CrossRef]
38. Vitorino, C.; Ribeiro, M.; Carolino, E.; Costa, J.P.; Ferreira, A. Evaluation of knee joint cartilage through T2 Mapping technique by Magnetic Resonance. In Proceedings of the 6th IEEE Portuguese Meeting on Bioengineering, ENBENG 2019-Proceedings, 2019, Lisbon, Portugal, 22–23 February 2019. [CrossRef]

39. Pedoia, V.; Norman, B.; Mehany, S.N.; Bucknor, M.D.; Link, T.M.; Majumdar, S. 3D convolutional neural networks for detection and severity staging of meniscus and PFJ cartilage morphological degenerative changes in osteoarthritis and anterior cruciate ligament subjects. *J. Magn. Reson. Imaging* **2019**, *49*, 400–410. [CrossRef]
40. Kubicek, J.; Krestanova, A.; Penhaker, M.; Augustynek, M.; Cerny, M.; Oczka, D. Modeling of Articular Cartilage with Goal of Early Osteoarthritis Extraction Based on Local Fuzzy Thresholding Driven by Fuzzy C-Means Clustering. In *Intelligent Information and Database Systems, Proceedings of the 11th Asian Conference, ACIIDS 2019, Yogyakarta, Indonesia, 8–11 April 2019*; Lecture Notes in Computer Science; Springer International Publishing: Berlin/Heidelberg, Germany, 2019; Volume 11432, pp. 289–299. [CrossRef]
41. Fang, L.; Wang, X. Dual-stream parallel model of cartilage injury diagnosis based on local centroid optimization. *Biomed. Signal Process. Control* **2023**, *80*, 104229. [CrossRef]
42. Joseph, G.B.; McCulloch, C.E.; Sohn, J.H.; Pedoia, V.; Majumdar, S.; Link, T.M. AI MSK clinical applications: Cartilage and osteoarthritis. *Skelet. Radiol.* **2022**, *51*, 331–343. [CrossRef]
43. Schiratti, J.-B.; Dubois, R.; Herent, P.; Cahané, D.; Dachary, J.; Clozel, T.; Wainrib, G.; Keime-Guibert, F.; Lalande, A.; Pueyo, M.; et al. A deep learning method for predicting knee osteoarthritis radiographic progression from MRI. *Arthritis Res. Ther.* **2021**, *23*, 262. [CrossRef]
44. Mahum, R.; Rehman, S.U.; Meraj, T.; Rauf, H.T.; Irtaza, A.; El-Sherbeeny, A.M.; El-Meligy, M.A. A novel hybrid approach based on deep cnn features to detect knee osteoarthritis. *Sensors* **2021**, *21*, 6189. [CrossRef] [PubMed]
45. George, Y.; Antony, B.J.; Ishikawa, H.; Wollstein, G.; Schuman, J.S.; Garnavi, R. Attention-Guided 3D-CNN Framework for Glaucoma Detection and Structural-Functional Association Using Volumetric Images. *IEEE J. Biomed. Health Inform.* **2020**, *24*, 3421–3430. [CrossRef] [PubMed]
46. Afara, I.O.; Sarin, J.K.; Ojanen, S.; Finnilä, M.A.J.; Herzog, W.; Saarakkala, S.; Korhonen, R.K.; Töyräs, J. Machine Learning Classification of Articular Cartilage Integrity Using Near Infrared Spectroscopy. *Cell. Mol. Bioeng.* **2020**, *13*, 219–228. [CrossRef]
47. Fujiwara, K.; Fang, W.; Okino, T.; Sutherland, K.; Furusaki, A.; Sagawa, A.; Kamishima, T. Quick and accurate selection of hand images among radiographs from various body parts using deep learning. *J. X-Ray Sci. Technol.* **2020**, *28*, 1199–1206. [CrossRef] [PubMed]
48. Mashyakhy, M.; Alkahtani, A.; Abumelha, A.; Sharroufna, R.; Alkahtany, M.; Jamal, M.; Robaian, A.; Binalrimal, S.; Chohan, H.; Patil, V.; et al. Taurine Augments Telomerase Activity and Promotes Chondrogenesis in Dental Pulp Stem Cells. *J. Pers. Med.* **2021**, *11*, 491. [CrossRef]
49. Su, Q.; Zhang, Y.; Zhang, Y.; Li, J.; Xue, C.; Ge, H.; Cheng, B. Multivariate Analysis of Associations between Patellofemoral Instability and Gluteal Muscle Contracture: A Radiological Analysis. *J. Pers. Med.* **2022**, *12*, 242. [CrossRef]
50. Kapur, J.N.; Sahoo, P.K.; Wong, A.K.C. A new method for gray-level picture thresholding using the entropy of the histogram. *Comput. Vis. Graph. Image Process.* **1985**, *29*, 273–285. [CrossRef]
51. Wang, Z.; Bovik, A.C.; Sheikh, H.R.; Simoncelli, E.P. Image quality assessment: From error visibility to structural similarity. *IEEE Trans. Image Process.* **2004**, *13*, 600–612. [CrossRef]
52. NIMH Data Archive-OAI (The Osteoarthritis Initiative). National Institutes of Health. U.S. Department of Health and Human Services. Available online: https://nda.nih.gov/oai/ (accessed on 10 January 2023).
53. Kuo, C.F.J.; Yang, Z.-X.; Lai, W.-S.; Liu, S.-C. Application of Image Processing and 3D Printing Technique to Development of Computer Tomography System for Automatic Segmentation and Quantitative Analysis of Pulmonary Bronchus. *Mathematics* **2022**, *10*, 3354. [CrossRef]
54. Maqsood, M.; Yasmin, S.; Mehmood, I.; Bukhari, M.; Kim, M. An Efficient DA-Net Architecture for Lung Nodule Segmentation. *Mathematics* **2021**, *9*, 1457. [CrossRef]
55. Saladi, S.; Karuna, Y.; Koppu, S.; Reddy, G.R.; Mohan, S.; Mallik, S.; Qin, H. Segmentation and Analysis Emphasizing Neonatal MRI Brain Images Using Machine Learning Techniques. *Mathematics* **2023**, *11*, 285. [CrossRef]